


A novel numerical strategy for modeling the moving boundary value problem of electrochemical machining

Tim van der Velden¹  | Stephan Ritzert¹ | Stefanie Reese¹ | Johanna Waimann²

¹Institute of Applied Mechanics, RWTH Aachen University, Aachen, Germany

²Junior Professorship for Modeling and Simulation Techniques for Systems of Polycrystalline Materials, Institute of Applied Mechanics, RWTH Aachen University, Aachen, Germany

Correspondence

Tim van der Velden, Institute of Applied Mechanics, RWTH Aachen University, Mies-van-der-Rohe-Str. 1, D-52074 Aachen, Germany.

Email:

tim.van.der.velden@ifam.rwth-aachen.de

Funding information

German Research Foundation (DFG), Grant/Award Numbers: 453715964, 223500200 (M05), 417002380 (A01)

Abstract

This work presents a new numerical approach to efficiently model the cathode's moving surface in the moving boundary value problem of electrochemical machining. Until recently, the process simulation with finite elements had the drawback of remeshing required by the changing surface geometries. This disadvantage was overcome by an innovative model formulation for the anodic dissolution that utilizes effective material parameters as well as the dissolution level as an internal variable and, thereby, does not require remeshing. Now, we suggest a new numerical method to model arbitrarily shaped and moving cathodes. Two methodologies are investigated to describe the time varying position of the cathode and compared in terms of implementational effort and numerical efficiency. In the first approach, we change the electric conductivity of elements within the cathode and, in a second approach, we apply Dirichlet boundary conditions on the nodes of corresponding elements. For both methods, elements on the cathode's surface are treated with effective material parameters. This procedure allows for the efficient simulation of industrially relevant, complex geometries without mesh adaptation. The model's performance is validated by means of analytical, numerical and experimental results from the literature. The short computation times make the approach interesting for industrial applications.

KEYWORDS

electrochemical machining, finite element method, moving boundary value problem

1 | INTRODUCTION

The industry's ever increasing need for the production of complex structures that consist of high strength materials propels the use of electrochemical machining (ECM).¹ A decisive advantage of the process is the possibility to machine solid materials with exceptional hardness at high removal rates. Moreover, being a contactless process, ECM does not lead to tool wear and does not afflict any mechanical damage to the rim zone of the workpiece. The process utilizes the effect of electrolysis to machine the workpiece by material dissolution.²⁻⁴

Figure 1 shows a schematic sketch for an arbitrarily shaped tool. A direct current is applied at the electrodes and yields an electric current at the workpiece's surface that causes the anodic dissolution.

This is an open access article under the terms of the [Creative Commons Attribution-NonCommercial-NoDerivs](https://creativecommons.org/licenses/by-nc-nd/4.0/) License, which permits use and distribution in any medium, provided the original work is properly cited, the use is non-commercial and no modifications or adaptations are made.

© 2022 The Authors. *International Journal for Numerical Methods in Engineering* published by John Wiley & Sons Ltd.

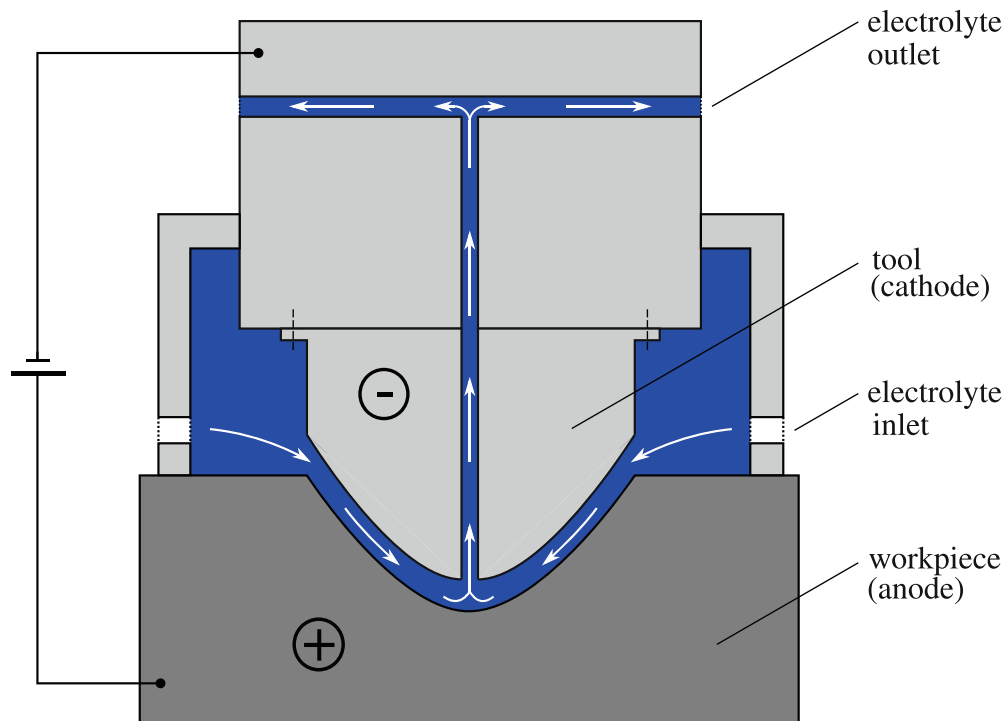


FIGURE 1 Illustration of the electrochemical machining process (after Reference 4).

The fields of application for ECM range from the blade production in turbomachinery manufacturing over the creation of shape optimized cooling bores for improved stress distributions to the precision machining of filigree structures.^{4,5} This wide range of applications motivates the development of efficient simulation methods. Since it is difficult to predict the final shape of the workpiece in ECM, simulations can help to reduce costly trial and error experiments and also to speed up the design process.⁶

Over time, different numerical methodologies were employed to model ECM: These are the finite difference method (e.g., References 7-9), the boundary element method (e.g., References 10,12,13, Hansen in References 11) and also the finite element method (FEM) (e.g., References 14-16) that is also employed in this work. According to Reference 6, the FEM possesses the drawback of computationally expensive remeshing due to the changing geometries. To circumvent remeshing, e.g., Reference 17 tried to delete and modify elements close to the anode's surface, which also proved to be expensive. An elegant procedure to adapt the mesh for moving interfaces was presented by Reference 18, who employ an elastic body analogy¹⁹ to realign the refined region of the mesh with the anodic surface.

However, even state of the art formulations like e.g. the one of Reference 20 that models precise ECM with pulsed current and oscillating cathode still need remeshing to model the anodic dissolution and the cathode movement by assigning separate domains for fluid and solid. To our best knowledge, previous models lack a continuous formulation of the dissolution process without the requirement of mesh adaption.

Therefore, we proposed a novel approach that works entirely without remeshing and models the anodic dissolution in ECM with effective material parameters and an internal variable.²¹ In this work, the novel approach based on effective material parameters serves to model the movement of arbitrarily shaped cathodes in ECM. Previous studies were restricted to a stationary cathode or a simplified modeling of the cathode feed. The aspiration to investigate industrially relevant and complex problems underlines the necessity of this contribution to efficiently and accurately model the cathode.

To this end, this work investigates two approaches for modeling the cathode. In method A, the electric conductivity of the elements within the cathode is modified. In method B, Dirichlet boundary conditions are applied on all nodes within the cathode. Both methodologies are based on effective material parameters for elements on the cathode's surface and, thereby, allow for a simulation entirely without remeshing.

Nowadays, following the earlier works of e.g. References 22,23, numerous authors investigate electrically coupled multifield problems. Reference 24 conduct for example, electro-chemo-mechanical simulations, Reference 25 additionally

include thermal and Reference 26 magnetic effects to name only a few. We, however, focus in this work on the modeling of the moving boundary value problem and, therefore, for simplicity, restrict ourselves to the electric field problem, since the electric current density is the driving force in electrochemical machining. The thermal field is thus assumed to be constant.

Outline of the work. In Section 2, the electric balance equation and the constitutive laws are introduced. Thereafter, we give a brief summary of the dissolution model in Section 3 and comment on numerical aspects in Section 4. In Section 5, we present the new methodologies for modeling the cathode. In Section 6.1, analytical reference solutions serve to validate the model's accuracy and additional studies regarding the runtime and the choice of the effective material parameters are conducted. In Sections 6.2 and 6.3, challenging examples with numerical and experimental references are investigated. In Section 6.4, the model's ability to model complex cathode shapes by simulating a blade machining process is confirmed. A conclusion is provided in Section 7.

Notational conventions. In this work, italic characters a , A denote scalars and zeroth-order tensors and bold-face italic characters \mathbf{b} , \mathbf{B} refer to vectors and first-order tensors and bold-face roman characters \mathbf{c} , \mathbf{C} refer to matrices and second-order tensors. The operators $\text{div}(\bullet)$ and $\text{grad}(\bullet)$ denote the divergence and gradient operation of a quantity with respect to Cartesian coordinates. A dot \cdot defines the single contraction of two tensors. The time derivative of a quantity is given by $(\dot{\bullet})$. A tilde $(\widetilde{\bullet})$ defines a prescribed quantity on the corresponding boundary. Moreover, Table 1 lists the relevant symbols and states, if applicable, the corresponding SI units.

TABLE 1 Relevant symbols

Symbol	Unit	Definition
ϵ_0	[A s/(V m)]	Electric constant
ϵ_r	[–]	Relative permittivity
λ_{cat}	[–]	Cathode ratio
v_{dis}	[m ³ /(A s)]	Effectively dissolved volume
ρ_E	[A s/m ³]	Electric volume charge density
\mathcal{A}	[–]	Activation function
d	[–]	Dissolution level
\mathbf{D}	[A s/m ²]	Electric displacement field
\mathbf{E}	[V/m]	Electric field strength
I	[A]	Electric current
\mathbf{j}	[A/m ²]	Electric current density
k_E	[A/(V m)]	Electric conductivity
\mathbf{n}	[–]	Normal vector
Q	[A s]	Electric charge
R	[V/A]	Electric resistance
t	[s]	Machining time
v	[V]	Electric potential
V_{cat}	[m ³]	Cathode volume
V_{dis}	[m ³]	Dissolved volume
V_{el}	[m ³]	Element volume
V_{ref}	[m ³]	Reference volume
\mathbf{x}	[m]	Position
$(\bullet)^{\text{CAT}}$		Cathode quantity
$(\bullet)^{\text{EL}}$		Electrolyte quantity
$(\bullet)^{\text{ME}}$		Metal quantity

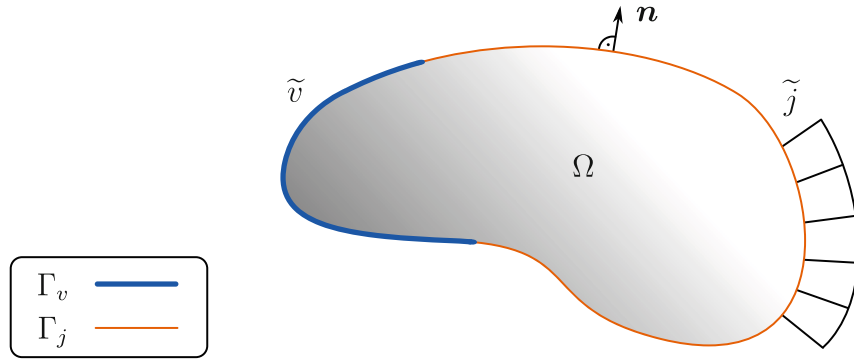


FIGURE 2 Illustration of the electric boundary value problem. The accentuated blue segment of the boundary on the left part of the body depicts the Dirichlet boundary Γ_v where the electric potential is prescribed according to \tilde{v} . On the remaining orange part of the boundary, Γ_j , either a prescribed electric current density \tilde{j} or zero flux conditions are applied (Neumann boundary).

2 | CONSTITUTIVE MODELING

The present contribution focuses on the modeling of moving cathode geometries. As mentioned in Section 1, we consider isothermal problems and, therefore, solely present the balance of electric charge including Dirichlet and Neumann boundary conditions (see Figure 2 and cf. Reference 27):

$$\begin{aligned} \dot{\rho}_E + \operatorname{div}(\mathbf{j}) &= 0 & \text{in } \Omega \\ v &= \tilde{v}(t) & \text{on } \Gamma_v \\ \mathbf{j} \cdot \mathbf{n} &= \tilde{j} & \text{on } \Gamma_j \end{aligned} \quad (1)$$

The primary variable of this problem is the electric potential v . The movement of the cathode's surface is incorporated by considering time varying Dirichlet boundary conditions $\tilde{v}(t)$ for the electric potential. The electric field strength \mathbf{E} , the electric displacement field \mathbf{D} and Gauss' law of electrostatics read

$$\mathbf{E} = -\operatorname{grad}(v), \quad \mathbf{D} = \epsilon_0 \epsilon_r \mathbf{E}, \quad \rho_E = \operatorname{div}(\mathbf{D}) \quad (2)$$

where ϵ_0 denotes the electric constant, ϵ_r the relative permittivity tensor, which reduces for the isotropic case to $\epsilon_r \mathbf{I}$ with the identity tensor \mathbf{I} , and ρ_E the electric volume charge density. The constitutive law of the electric current density \mathbf{j} yields

$$\mathbf{j} = \mathbf{k}_E \mathbf{E} \quad (3)$$

where \mathbf{k}_E denotes the electric conductivity tensor, which simplifies in the isotropic context to $k_E \mathbf{I}$. Finally, the weak form g_v may be obtained from Equation (1-1) by multiplying with an arbitrary test function δv , integrating over the domain Ω , considering the integration by parts as well as the definitions of Equation (2)

$$g_v := - \int_{\Omega} (\epsilon_0 \epsilon_r \dot{\mathbf{E}} + \mathbf{k}_E \mathbf{E}) \cdot \operatorname{grad}(\delta v) dV + g_j = 0 \quad (4)$$

where $\dot{\mathbf{E}}$ is the time derivative of the electric field strength \mathbf{E} and g_j the virtual work resulting from a prescribed electric current density on Γ_j . For the derivation of Equation (4), the interested reader is kindly referred to the appendix.

3 | ANODIC DISSOLUTION

This work utilizes the model of Reference 21 to describe the anodic dissolution. Analogously to damage modeling (e.g., Reference 28), an internal variable in combination with effective material parameters serves to describe the transition from an undissolved material state to a fully dissolved one. In the first situation, there is only metal present. In the second

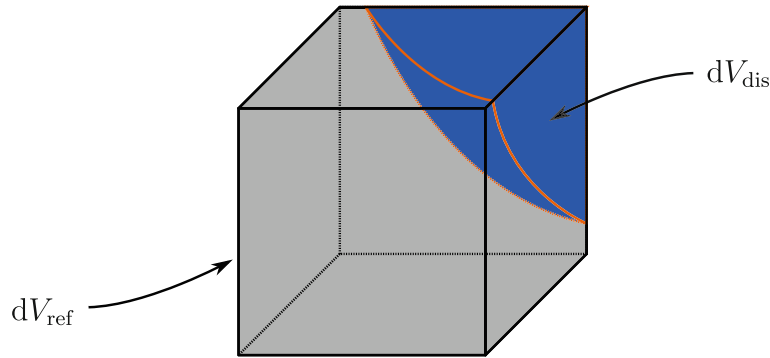


FIGURE 3 Visualization of the reference volume dV_{ref} and the incremental dissolved volume dV_{dis} . The orange line surrounds the anode's surface.

situation, the metallic material has been fully dissolved such that only electrolyte remains. The dissolution level $d \in [0, 1]$ states the ratio $d = dV_{\text{dis}}/dV_{\text{ref}}$ of the incremental dissolved volume dV_{dis} to the volume of the corresponding reference volume dV_{ref} (see Figure 3). Hence, the rate of the dissolution level yields the relation

$$\dot{d} \, dV_{\text{ref}} = d\dot{V}_{\text{dis}} \quad (5)$$

where it is assumed that dV_{ref} is constant over time. In the formulation, we employ a modified version of Faraday's law of electrolysis to correlate the dissolved volume with the passing electric charges.⁴ Using the material parameter ν_{dis} that represents the dissolved volume per electric charge, and the activation function \mathcal{A} as well as the time derivative of the incremental electric charge $d\dot{Q}$, the time derivative of the incrementally dissolved volume reads

$$d\dot{V}_{\text{dis}} = \nu_{\text{dis}} \mathcal{A} \, d\dot{Q}. \quad (6)$$

Moreover, we consider the definition of the activation function

$$\mathcal{A}(\mathbf{x}, t) = \begin{cases} 1, & \text{contact metal-electrolyte} \\ 0, & \text{else} \end{cases} \quad (7)$$

that depends on the position \mathbf{x} and time t and indicates whether the material has contact with the electrolyte which is a requirement for the chemical reaction. Further, the connection between the time derivative of the incremental electric charge $d\dot{Q}$ and the incremental electric current dI is given as

$$d\dot{Q} = dI, \quad (8)$$

where $dI(\mathbf{j}, d)$ depends on the electric current density \mathbf{j} and the dissolution level d . In general, the electric current I passing through a surface segment S is computed from \mathbf{j} (see e.g. Reference 29) by

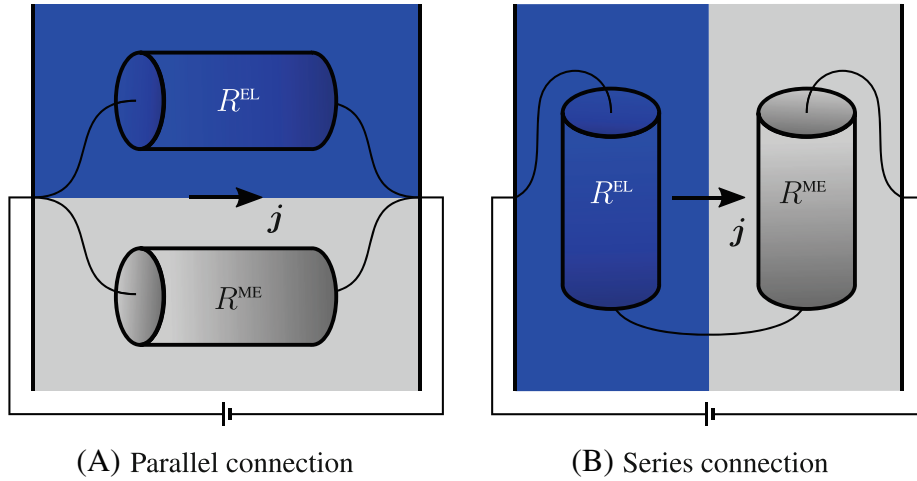
$$I = \int_S \mathbf{j} \cdot \mathbf{n} \, dA \quad (9)$$

and defines the number of electric charges Q that move through S per unit time. For the specific function of $dI(\mathbf{j}, d)$ the reader is kindly referred to Reference 21. With Equation (8), we accordingly rewrite Equation (5) to

$$\dot{d} \, dV_{\text{ref}} = \nu_{\text{dis}} \mathcal{A}(\mathbf{x}, t) \, dI(\mathbf{j}, d). \quad (10)$$

Finally, we define the effective material parameters. Previously, the volume average of metal and electrolyte properties (Figure 4A) was considered to read

$$(\bullet)^{\text{p}} = (1 - d) (\bullet)^{\text{ME}} + d (\bullet)^{\text{EL}}. \quad (11)$$



(A) Parallel connection

(B) Series connection

FIGURE 4 Parallel (A) and series connection (B): Depending on the rule of mixture, different electrical circuits for a horizontal electric current density j passing between the electrodes through the electrical resistances R^{ME} and R^{EL} are considered.

This constitutes a parallel connection for the rule of mixture. Motivated by the analogy of electrical circuits (Figure 4), this work additionally considers a series connection (Figure 4B) for the rule of mixture between metal and electrolyte:

$$(\bullet)^s = \left[(1 - d) / (\bullet)^{ME} + d / (\bullet)^{EL} \right]^{-1} \quad (12)$$

In Section 6.1, the influence of the rule of mixture on the dissolved volume is studied.

4 | NUMERICAL ASPECTS

For the time and spatial discretization, we employ the backward Euler method and the finite element method, respectively. For detailed information on the latter, the reader is kindly referred to References 30 and 31. The time discretization yields

$$\dot{E} = \frac{E_{n+1} - E_n}{\Delta t} \quad (13)$$

where $(\bullet)_{n+1}$ and $(\bullet)_n$ denote the values of the current and the previous time step.

4.1 | Linearization

Considering the time discretization of Equation (13), we linearize the weak form in Equation (4) with respect to the primary variable v_{n+1} . For the later presented simulation of the ECM process, we neglect the contribution from g_j in Equation (4), since we focus in this work on prescribing Dirichlet boundary conditions and apply solely zero flux conditions. Then, the linearization of g_v about a known state (\bar{v}_{n+1}) reads

$$L_{g_v} = g_v(\bar{v}_{n+1}, \delta v) + \Delta_v g_v(\bar{v}_{n+1}, \delta v, \Delta v_{n+1}) \stackrel{!}{=} 0 \quad \forall \delta v \quad (14)$$

and with

$$E_{n+1}(\alpha) = \bar{E}(\bar{v}_{n+1}) + \alpha \Delta E(\Delta v_{n+1}) \quad (15)$$

the Gâteaux-derivative is computed by

$$\begin{aligned}
\Delta_v g_v &= \frac{d}{d\alpha} \left[- \int_{\Omega} \left(\epsilon_0 \bar{\epsilon}_r \dot{\mathbf{E}}_{n+1}(\alpha) + \bar{k}_E \mathbf{E}_{n+1}(\alpha) \right) \cdot \text{grad}(\delta v) dV \right]_{\alpha=0} \\
&= \left[- \int_{\Omega} \left(\epsilon_0 \bar{\epsilon}_r \frac{\partial \dot{\mathbf{E}}_{n+1}(\alpha)}{\partial \alpha} + \bar{k}_E \frac{\partial \mathbf{E}_{n+1}(\alpha)}{\partial \alpha} \right) \cdot \text{grad}(\delta v) dV \right]_{\alpha=0} \\
&= - \int_{\Omega} \left(\epsilon_0 \bar{\epsilon}_r \frac{1}{\Delta t} + \bar{k}_E \right) \Delta \mathbf{E} \cdot \text{grad}(\delta v) dV
\end{aligned} \tag{16}$$

where the simplifications for the permittivity and conductivity tensors as well as a general rule of mixture $(\bar{\bullet}) := (\bullet)(d_n)$ with a staggered treatment of the dissolution level d are already considered.

4.2 | Finite element discretization

Thereafter, the problem is discretized in space using the finite element method. First, the domain Ω is approximated by n_{el} finite elements

$$\Omega \approx \Omega^h = \bigcup_{e=1}^{n_{\text{el}}} \Omega^e. \tag{17}$$

Then, the electric potential v and its variation δv are approximated by tri-linear shape functions stored in the shape function row vector \mathbf{N}_v^e

$$(\delta)v(\mathbf{x}) \approx (\delta)v^e(\mathbf{x}) = \mathbf{N}_v^e(\mathbf{x}) (\delta)\mathbf{v}^e, \quad \mathbf{x} \in \Omega^e \tag{18}$$

and their gradients accordingly by the corresponding derivatives of the shape functions stored in the matrix of the spatial derivatives \mathbf{B}_v^e

$$\text{grad}((\delta)v(\mathbf{x})) \approx \text{grad}((\delta)v^e(\mathbf{x}))^e = \mathbf{B}_v^e(\mathbf{x}) (\delta)\mathbf{v}^e, \quad \mathbf{x} \in \Omega^e. \tag{19}$$

where $(\delta)\mathbf{v}^e$ denote the column vectors of the nodal values of the finite element e . The interpolations (Equations 18 and 19) are inserted into the linearization (Equation 14) and added over all elements yielding

$$\sum_{e=1}^{n_{\text{el}}} \delta \mathbf{v}^{eT} \left\{ \left[\mathbf{c}_{vv}^e + \mathbf{k}_{vv}^e \right] \Delta \mathbf{v}_{n+1}^e \right\} = \sum_{e=1}^{n_{\text{el}}} - \delta \mathbf{v}^{eT} \left\{ \mathbf{r}_v^e \right\} \tag{20}$$

with the element matrices \mathbf{c}_{vv}^e and \mathbf{k}_{vv}^e and the element residual vector \mathbf{r}_v^e :

$$\mathbf{c}_{vv}^e = \int_{\Omega^e} \mathbf{B}_v^{eT} \left(\epsilon_0 \bar{\epsilon}_r \frac{1}{\Delta t} \right)^e \mathbf{B}_v^e dV^e \tag{21}$$

$$\mathbf{k}_{vv}^e = \int_{\Omega^e} \mathbf{B}_v^{eT} \left(\bar{k}_E \right)^e \mathbf{B}_v^e dV^e \tag{22}$$

$$\mathbf{r}_v^e = \int_{\Omega^e} \mathbf{B}_v^{eT} \left(\epsilon_0 \bar{\epsilon}_r \dot{\mathbf{E}} + \bar{k}_E \mathbf{E} \right)^e dV^e \tag{23}$$

The formulation is implemented into the finite element software FEAP.³² The activation function \mathcal{A} (Equation 7) is incorporated into the solution algorithm by an update procedure at the end of every time step. When a finite element dissolves completely, it triggers the update procedure and activates all adjacent metal elements that have a shared surface with the dissolved element. The cut-off volume V_{co} , which was investigated in Reference 21, denotes the theoretically dissolved volume in an integration point that is neglected when $d_{n+1} > 1$ is reset to $d_{n+1} = 1$. In the present formulation, V_{co} is allocated to the activated elements. Thereby, the formulation allows for the use of larger time steps and, hence, reduces computation time.

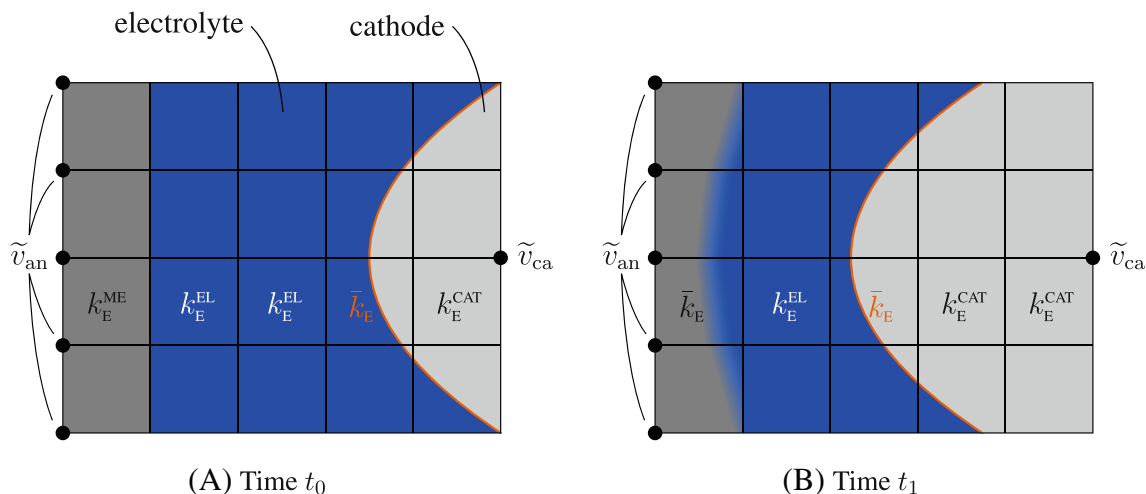


FIGURE 5 Illustration of method A. The cathode moves towards the anode from time t_0 to time t_1 . The electric potential v is fixed at one node within the cathode and the cathode feed is modeled by assigning each element within the cathode an infinite electric conductivity k_E^{CAT} . Exemplarily, the electric conductivity in a horizontal line of elements is shown at t_0 and t_1 and a black dot denotes a fixed degree of freedom.

5 | CATHODE MODELING

The driving force of the electric current is the potential difference Δv which is applied between cathode and anode. The domain of the cathode is characterized by the property $v = 0$. To describe moving cathode geometries with arbitrary shapes, the model has to account for the time varying Dirichlet boundary conditions $\tilde{v}(t)$, i.e. to prescribe a zero electric potential on the surface and within the tool's geometry. Here, it is particularly advantageous that the new modeling approach does not require any mesh adaptation during the simulation despite the time dependent boundary conditions.

5.1 | Method A

Two different methods are employed to model the aforementioned condition. In the first, method A, the electric conductivities of the finite elements within the cathode are modified and the corresponding values are set numerically to infinity (Figure 5). The electric resistance of these elements is numerically zero and no change of the electric potential can be observed within the cathode. Thus, the equipotential line with $v = 0$ coincides with the cathode's surface as long as the electric potential v is prescribed at one point within the cathode. The advantage of method A is the straightforward implementation, since no modification of the global system of equations is required. This approach is inspired by Reference 16 who assign to each element a different material type depending on its classification as tool, workpiece or electrolyte.

5.2 | Method B

In the second, method B, a zero electric potential is applied directly on all nodes within the cathode (Figure 6). To account for the cathode feed, this approach requires an adaptation and a renumbering of the global system of equations in every time step. However, this procedure is computationally still beneficial, since the number of degrees of freedom reduces for regular cathode geometries steadily throughout the simulation when the number of fixed degrees of freedom inside the cathode increases. Furthermore, method B allows for the investigation of special cathode shapes, e.g. electrochemical wirecutting where the zero electric potential is defined only in the thin wire domain.

5.3 | Effective material parameters

Both models follow the conceptual approach of the dissolution model and work for a constant finite element mesh. Naturally, the cathode's surface does not necessarily coincide with the finite elements' edges. Thus, elements exist that

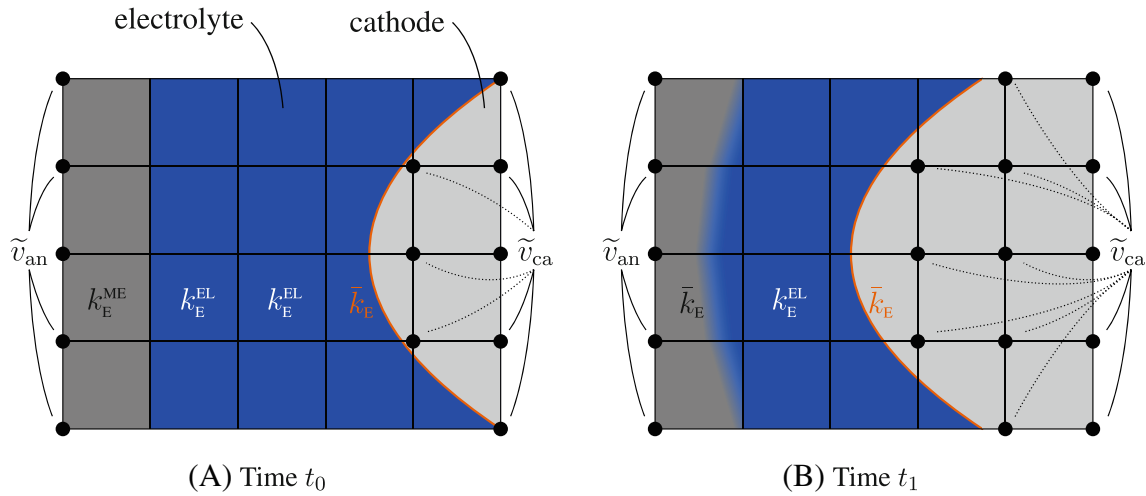


FIGURE 6 Illustration of method B. The cathode moves towards the anode from time t_0 to time t_1 . The electric potential v is fixed at all nodes within the cathode and the cathode feed is modeled by assigning additional Dirichlet boundary conditions. A black dot denotes a fixed degree of freedom.

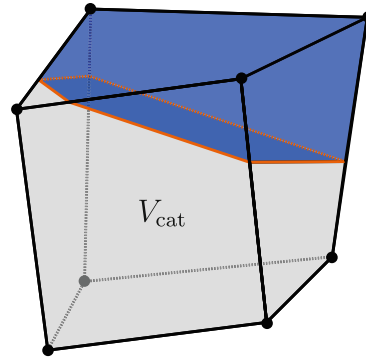


FIGURE 7 A finite element that is partially cathode and partially electrolyte. V_{cat} defines the finite element's volume inside the cathode and the orange line surrounds the cathode's surface.

are partially electrolyte and partially cathode (see Figure 7). Analogously to the dissolution level d , we define the cathode ratio

$$\lambda_{\text{cat}} = \frac{V_{\text{cat}}}{V_{\text{el}}} \quad (24)$$

that states the volume of the cathode in a finite element V_{cat} compared to the total volume of this element V_{el} . The polyeder's volume V_{cat} is computed via tetrahedralization using a Delaunay triangulation algorithm developed by Reference 33. Moreover, following the definition of Equations (11) and (12), we define the effective material parameters of partial cathode elements for a parallel connection as

$$(\bullet)^{\text{p}} = (1 - \lambda_{\text{cat}}) (\bullet)^{\text{EL}} + \lambda_{\text{cat}} (\bullet)^{\text{CAT}} \quad (25)$$

and for a series connection respectively as

$$(\bullet)^{\text{s}} = \left[(1 - \lambda_{\text{cat}}) / (\bullet)^{\text{EL}} + \lambda_{\text{cat}} / (\bullet)^{\text{CAT}} \right]^{-1} \quad (26)$$

where $(\bullet)^{\text{EL}}$ again denotes the material parameters of the electrolyte and $(\bullet)^{\text{CAT}}$ those of the cathode.

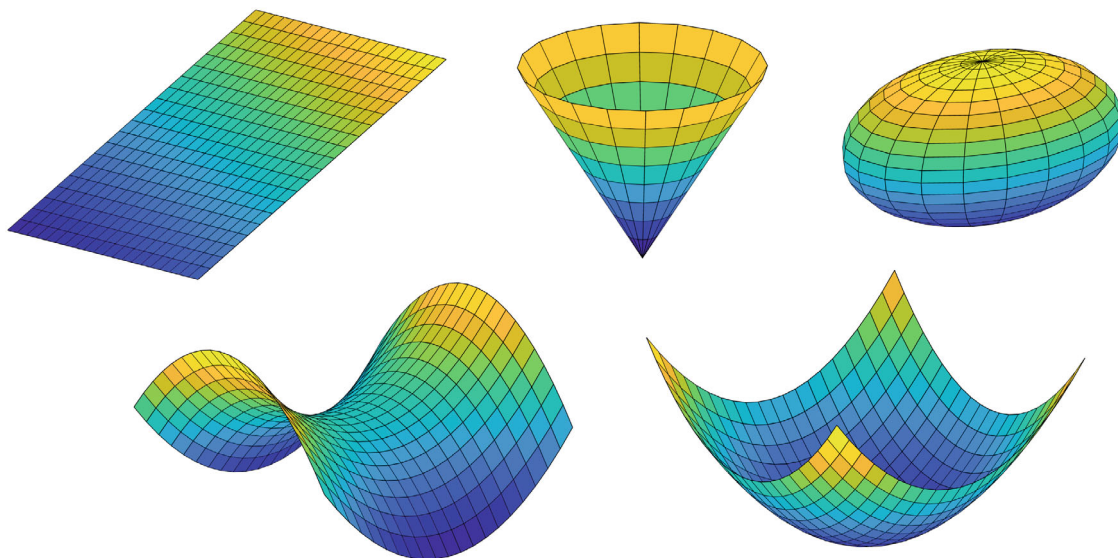


FIGURE 8 Basic geometries used for the cathode assembly: Plane, cone, ellipsoid and paraboloids.

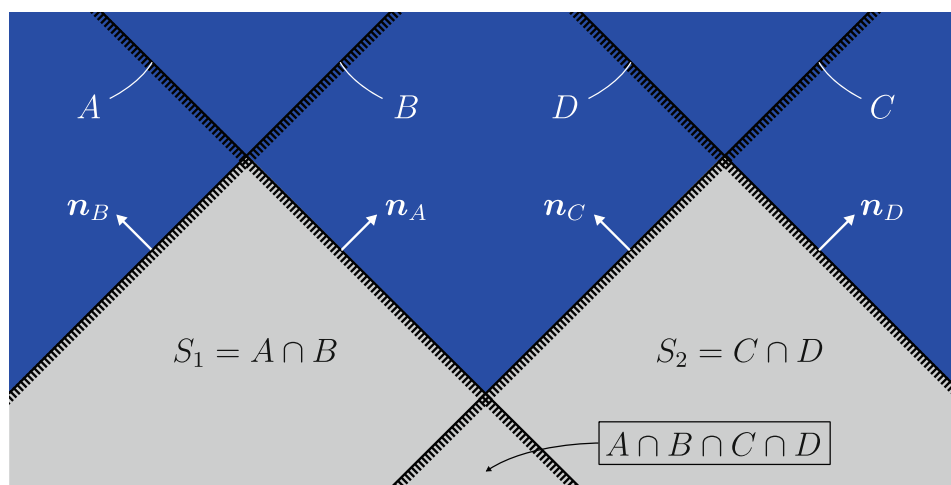


FIGURE 9 Illustration of a cathode assembly by conjunction (intersection) and disjunction (union). The subsets S_1 and S_2 are obtained by the conjunction of set A and B and set C and D , respectively. The disjunction of all subsets ($S_1 \cup S_2$) yields the total cathode geometry. A conjunction of set A , B , C and D without the definition of subsets would yield a different cathode geometry ($A \cap B \cap C \cap D \neq S_1 \cup S_2$).

The mathematical description of the cathode geometry follows set theory. Figure 8 shows different basic geometries that can be combined by conjunction in subsets. These subsets are combined by disjunction to obtain the total cathode geometry (see Figure 9). This two step procedure is necessary to fulfill the distributive property of disjunctions over conjunctions. The position vector which is inherent in each geometry models the cathode feed by incrementally updating its coordinates in every time step. The implementation features also additional options like the rotation of a geometry or the consideration of either the enclosed volume of a geometry or the volume outside of a geometry.

In a previous work, the theorem of intersecting lines served to model the cathode feed by a simplified approach. However, this procedure was restricted to processes with planar cathodes where the initial working gap width coincided with the gap width of the dynamic equilibrium state for a given feed rate. The new methodology allows for the investigation of arbitrary processes with varying process parameters as shown in Section 6.

Figure 10, finally, provides the resulting set of equations for the presented model.

- Balance equation and boundary conditions

$$\begin{aligned} \dot{\rho}_E + \operatorname{div}(\mathbf{j}) &= 0 & \text{in } \Omega & & \rho_E &= \operatorname{div}(\mathbf{D}) \\ v &= \tilde{v}(t) & \text{on } \Gamma_v & & \text{with } \mathbf{D} &= \epsilon_0 \bar{\epsilon}_r \mathbf{E} \\ \mathbf{j} \cdot \mathbf{n} &= \tilde{j} & \text{on } \Gamma_j & & \mathbf{E} &= -\operatorname{grad}(v) \end{aligned}$$

- Constitutive law

$$\mathbf{j} = \bar{k}_E \mathbf{E}$$

- Effective material parameters anode

$$\begin{aligned} (\bar{\bullet})^P &= (1 - d) (\bullet)^{\text{ME}} + d (\bullet)^{\text{EL}} \\ (\bar{\bullet})^S &= [(1 - d) / (\bullet)^{\text{ME}} + d / (\bullet)^{\text{EL}}]^{-1} \end{aligned}$$

- Effective material parameters cathode

$$\begin{aligned} (\bar{\bullet})^P &= (1 - \lambda_{\text{cat}}) (\bullet)^{\text{EL}} + \lambda_{\text{cat}} (\bullet)^{\text{CAT}} \\ (\bar{\bullet})^S &= [(1 - \lambda_{\text{cat}}) / (\bullet)^{\text{EL}} + \lambda_{\text{cat}} / (\bullet)^{\text{CAT}}]^{-1} \end{aligned}$$

FIGURE 10 Resulting set of equations for the moving boundary value problem.

TABLE 2 Material parameters and physical constants

Symbol	Unit	Value
k_E^{CAT}	[A/(V m)]	1.000×10^{12}
k_E^{EL}	[A/(V m)]	1.600×10^1
k_E^{ME}	[A/(V m)]	4.625×10^6
ϵ_r^{CAT}	[-]	1.000×10^0
ϵ_r^{EL}	[-]	8.000×10^1
ϵ_r^{ME}	[-]	1.000×10^0
ϵ_0	[A s/(V m)]	8.854×10^{-12}
ν_{dis}	[m ³ /(A s)]	1.000×10^{-11}

6 | NUMERICAL EXAMPLES

In this section, we employ the previously developed methodology to model the cathode feed in different applications. Furthermore, we compare the runtimes of method A and B. Analytical and experimental reference solutions serve to validate the methodology's performance and accuracy. Finally, we investigate an electrochemical blade manufacturing process. The presented model has been implemented in a three-dimensional finite-element formulation. For simplicity, only quasi two-dimensional examples have been investigated that were discretized by one element in thickness direction.

The material parameters employed in the simulations stem from Table 2, if not explicitly stated otherwise, and were selected with the help of the subproject F03 of the transregional Collaborative Research Center 136 "Process Signatures" and in line with the first example of Reference 21^{*†}. For simplicity, we consider only isothermal problems with a constant temperature of 50°C.

6.1 | Planar cathode - analytical validation

In the first example, we discuss a planar cathode (see Figure 11) with an analytical reference solution analogously to Reference 21. The dimensions read $l = h = 1$ mm with a thickness of 0.1 mm and a constant feed rate of $\dot{x}_{ca} = 0.01$ mm/s is employed with a potential difference of $\Delta v = 20$ V.

At the beginning, we utilize an initial working gap width of $s_{init} = 0.32$ mm that equals the gap width of the dissolution process in the dynamic equilibrium state (cf. Reference 4). Figure 12 shows the comparison of the parallel (Equations 11 and 25) the series connection (Equations 12 and 26). The dissolved volume of the finite element simulation after 60 s, which is normalized with respect to the analytical solution, is given for different time increments and element densities. Structured meshes are employed.

Although the results of the parallel connection converge against the analytical solution for fine meshes, they still show an error of +1.8 % for the finest discretization. The electric resistance of a dissolving element is underestimated by the parallel connection in this application, since the electric charges do not necessarily pass the electrolyte resistance in these elements (cf. Figure 4). Thereby, the electric current and the dissolved volume are overestimated by the model. The series

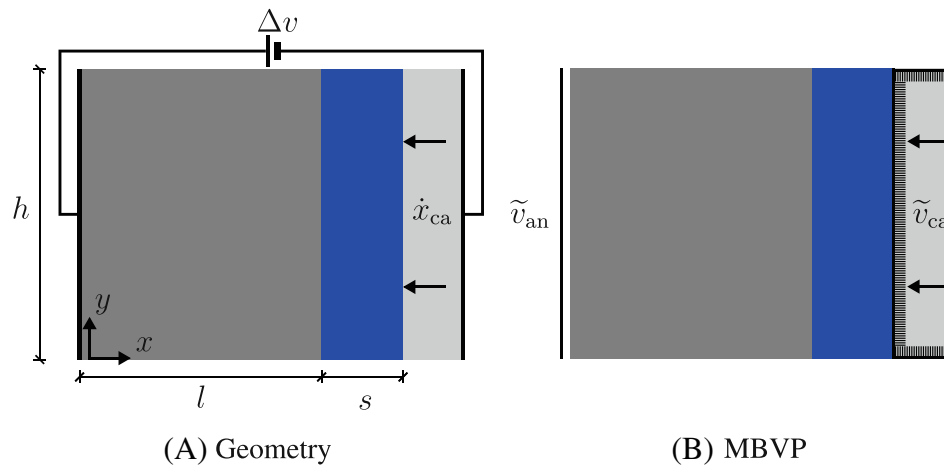


FIGURE 11 Geometry and moving boundary value problem for a planar cathode.

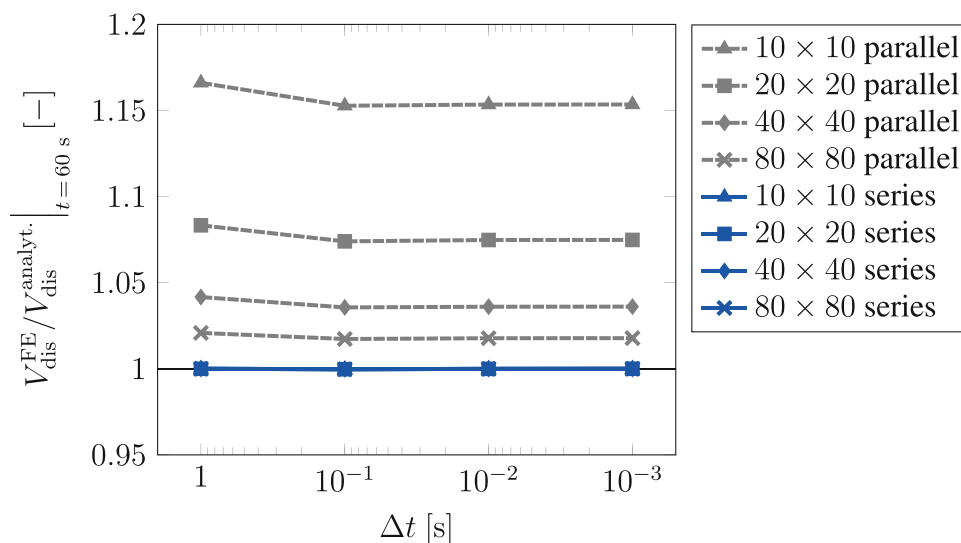


FIGURE 12 Comparison of the dissolved volume at $t = 60$ s of the finite element simulation and the analytical solution for the parallel and series connection with structured meshes for different element densities per mm^2 . The simulations with method A and B yield the same results.

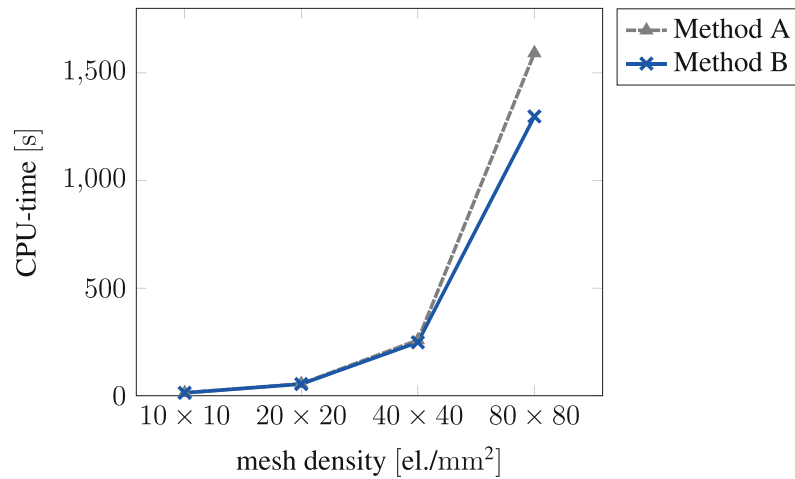


FIGURE 13 Comparison of the runtime of method A and B. Structured meshes are employed with the series connection and a time increment of $\Delta t = 10^{-1}$ s.

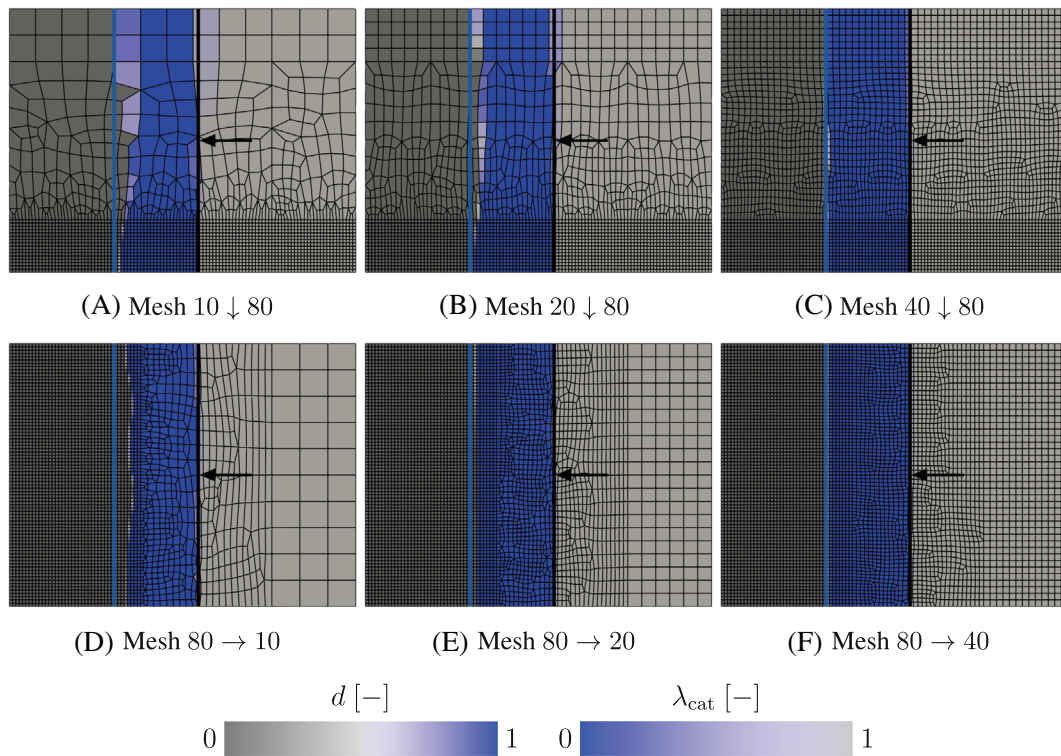


FIGURE 14 The dissolution level d and the cathode ratio λ_{cat} for distorted meshes at $t = 60$ s. The time increment reads $\Delta t = 10^{-3}$ s and the series connection as well as method B are employed. The vertical blue line provides the anode's surface according to the analytical reference solution. The vertical black line indicates the cathode surface's position and the black arrow gives the direction of the cathode feed.

connection, however, yields the correct solution regardless of the time step size and element density. Moreover, method A and B yield identical results.

Next, the runtime of method A and B are compared in Figure 13. The coarser meshes, which have fewer degrees of freedom compared to the fine meshes, yield similar runtimes for both methods. Nevertheless for the finest mesh, method B is 18.5 % faster, since the reduction of the size of the global system of equations yields a significant impact on the computational efficiency. Afterwards, we investigate this example using vertically and horizontally distorted meshes which stem from Reference 21. Figure 14 shows the results for the series connection and method B with $\Delta t = 10^{-3}$ s.

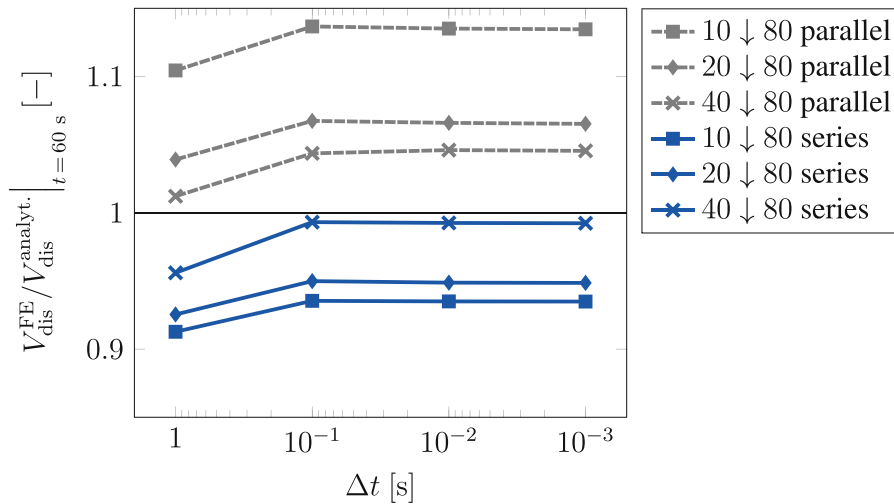


FIGURE 15 Comparison of the dissolved volume at $t = 60$ s of the finite element simulation using method B and the analytical solution for the parallel and series connection with vertically distorted meshes.

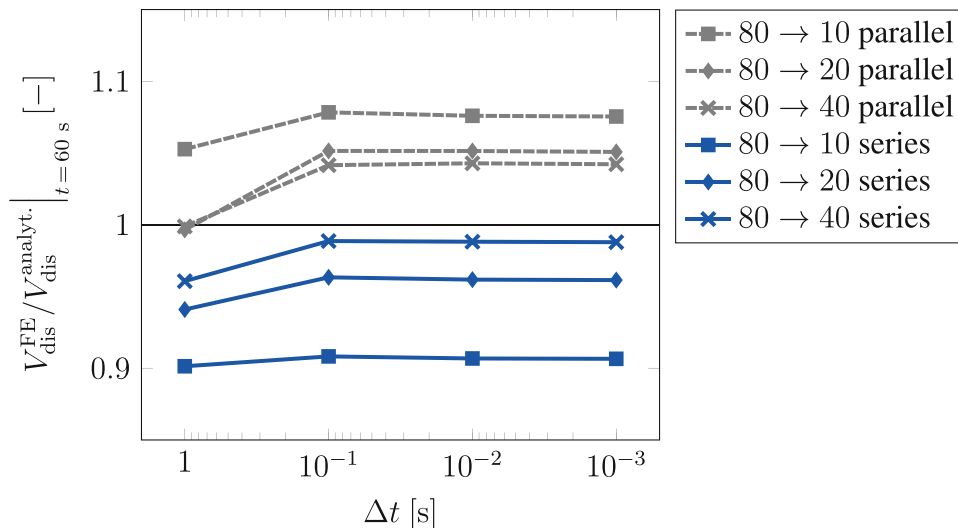


FIGURE 16 Comparison of the dissolved volume at $t = 60$ s of the finite element simulation using method B and the analytical solution for the parallel and series connection with horizontally distorted meshes.

For the most severe distortions, the dissolved volume is underestimated in the simulation (mesh 10 ↓ 80: −6.5 %, mesh 80 → 10: −9.3 %). However, the results improve for moderate distortions (mesh 20 ↓ 80: −5.1 %, mesh 80 → 20: −3.9 %) and converge towards the analytical solution for minor distortions (mesh 40 ↓ 80: −0.8 %, mesh 80 → 40: −1.2 %).

Figures 15 and 16 show the comparison of the parallel and series connection for different time step sizes. Both rules of mixture yield for all meshes already with the second largest time increment a stable solution that changes only marginally with a further reduction of the time increment. The parallel connection yields for the fine meshes with $\Delta t = 1$ s a solution close to the analytical result. However, this is not the model's final outcome, since convergence with respect to the time step size is not yet obtained. In the end, the dissolved volume is overestimated by the parallel connection for the different configurations and it yields also for minor distortions still an error of +4.5 % (mesh 40 ↓ 80) and +4.2 % (mesh 40 → 80). Based on these results, the remaining examples utilize the series connection as rule of mixture.

To demonstrate the flexibility of the new approach, Figure 17 shows the evolution of the working gap width s during the machining process with a constant feed rate $\dot{x}_{ca} = 0.015$ mm/s and varying initial widths s_{init} . All graphs concur at the analytical solution of $s = 0.213$ mm and confirm the correct operation of the method, since the convergence of the gap widths requires the exact modeling of the cathode.

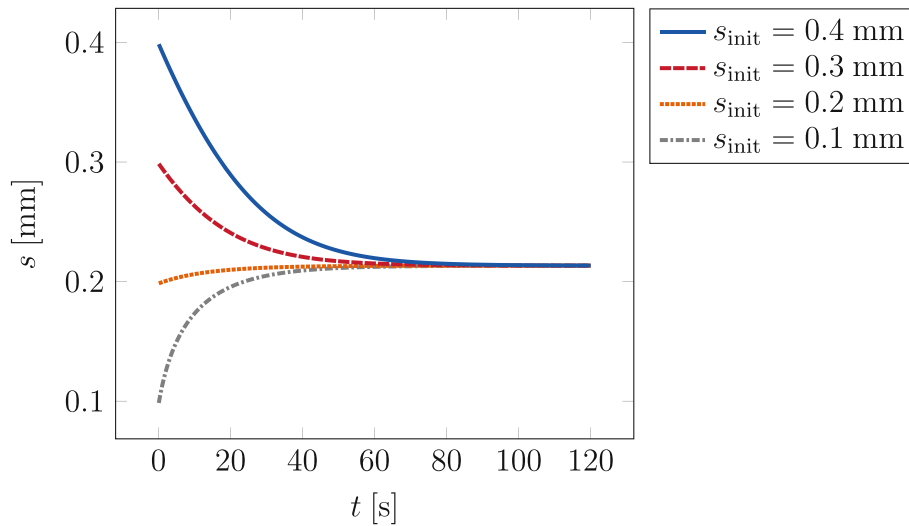


FIGURE 17 Investigation of the evolution of the working gap width s for different initial widths s_{init} . The feed rate is constant at $\dot{x}_{\text{ca}} = 0.015$ mm/s, $\Delta t = 0.1$ s and method B is employed.

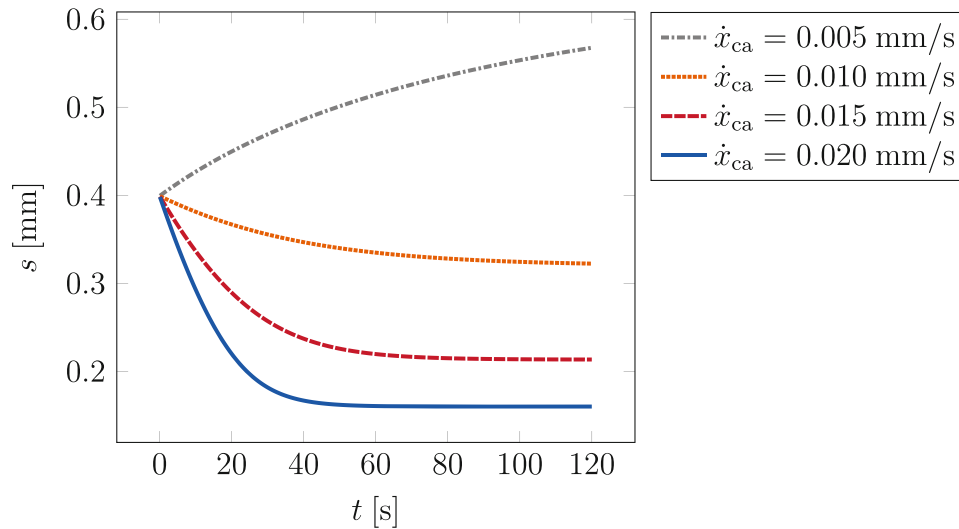


FIGURE 18 Investigation of the evolution of the working gap width s for different feed rates \dot{x}_{ca} . The initial width is $s_{\text{init}} = 0.4$ mm, $\Delta t = 0.1$ s and method B is employed.

Furthermore, Figure 18 shows the evolution of the gap width s for the same initial value s_{init} but different feed rates \dot{x}_{ca} . For a higher feed rate, the gap width decreases (cf. Reference 4) until it reaches the dynamic equilibrium state ($\dot{x}_{\text{ca}} = 0.010 - 0.020$ mm/s). For a lower feed rate, the working gap widens ($\dot{x}_{\text{ca}} = 0.005$ mm/s). This study again confirms the versatility of the new framework.

6.2 | Parabolic cathode - Hardisty and Mileham³⁴

In the second example, we consider a parabolically shaped cathode (Figure 19) which has formerly been studied by Reference 34. The material parameters read $k_{\text{E}}^{\text{ME}} = 6.670 \times 10^6$ A/(V m), $k_{\text{E}}^{\text{EL}} = 15$ A/(V m) and $v_{\text{dis}} = 3.696 \times 10^{-11}$ m³/(As). The cathode moves with a constant feed rate $\dot{x}_{\text{ca}} = 0.0145$ mm/s towards the anode with $\Delta t = 0.34483$ s yielding a displacement of 0.005 mm per time step and a total displacement of 2.5 mm after 500 time steps. The geometric dimensions are $l = 2$ mm, $h_1 = 3$ mm, $h_2 = 1.5$ mm, $s = 0.5$ mm with a thickness of 0.5 mm. The parabola is defined by the function

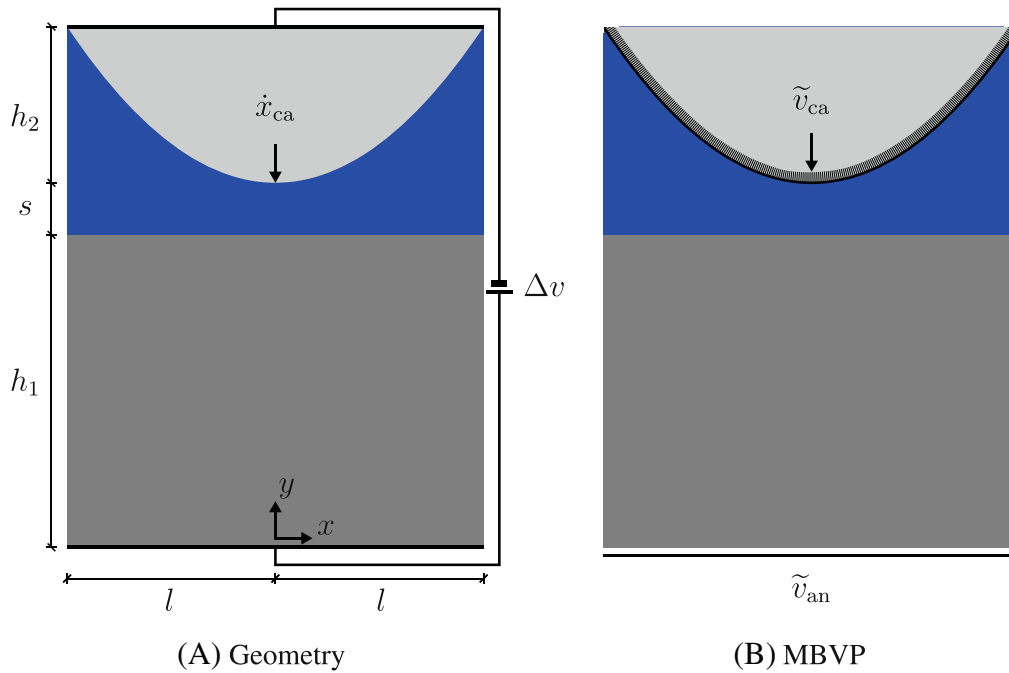


FIGURE 19 Geometry and moving boundary value problem for a parabolic cathode (cf. Reference 34).

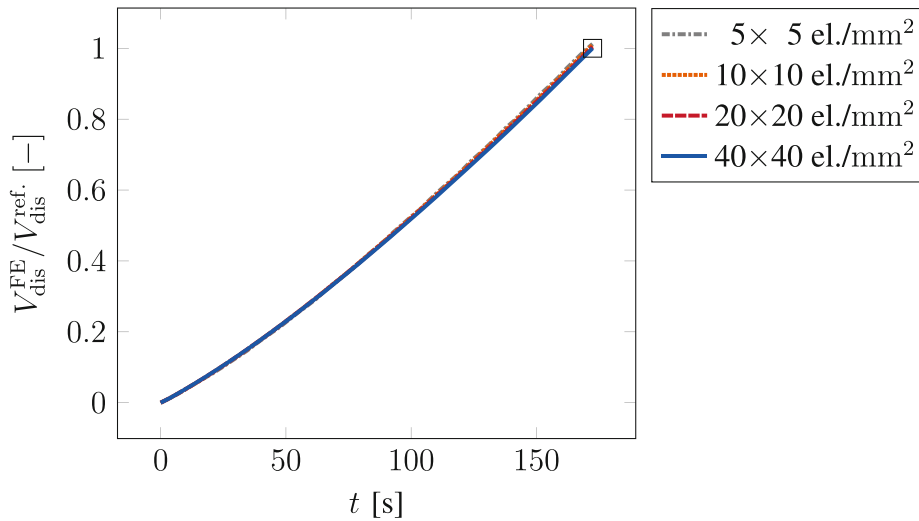


FIGURE 20 The dissolved volume over time computed with method B for different mesh densities. The graphs are normalized to the solution of the finest mesh with $\Delta t = 0.34483$ s. The black box indicates the point of comparison in Figure 21.

$f(x) = 0.375x^2 + 3.5$ and the potential difference is $\Delta v = 10$ V. Due to symmetry, only the left part $x \in [-2, 0]$ is simulated. We use structured meshes with finite element (el.) discretizations from 5×5 el./mm² to 40×40 el./mm².

Figure 20 shows the dissolved volume over time for the different mesh densities normalized to the solution of the finest mesh with $V_{\text{dis}}^{\text{ref.}} = 0.775$ mm³. The curves agree well and mesh convergence is proven.

In Figure 21, we compare the shape of the anode at the end of the simulation for different mesh discretizations. With finer discretizations, the surface profile becomes smoother. Nevertheless, already the coarsest discretization allows for an accurate prediction of the final work piece shape. The working gap width at the axis of symmetry at the end of the simulation is $s = 0.345$ mm and agrees with the reference solution of Reference 34 of $s^{\text{ref.}} = 0.35$ mm. These results confirm the model's capabilities to accurately predict the shape of the machined workpiece using coarse meshes.

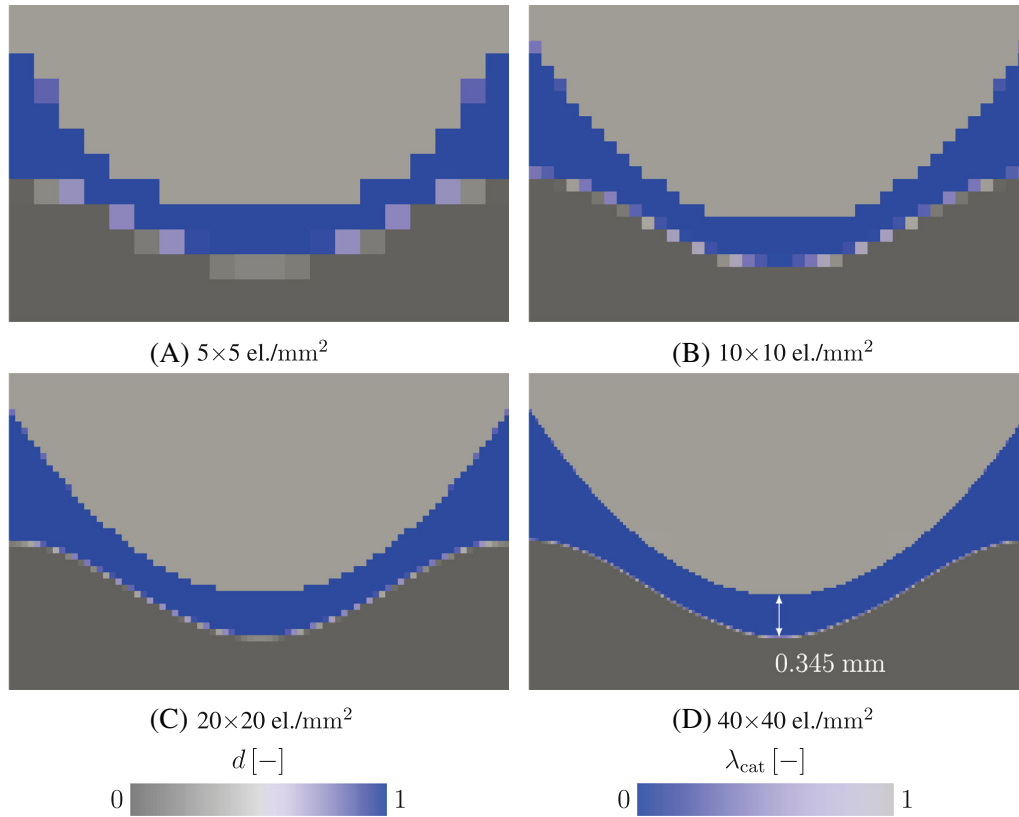


FIGURE 21 Zoom to the tool tip at the end of the simulation: The dissolution level d and the cathode ratio λ_{cat} show mesh convergence from coarse (Figure 21A) to fine mesh discretizations (Figure 21D).

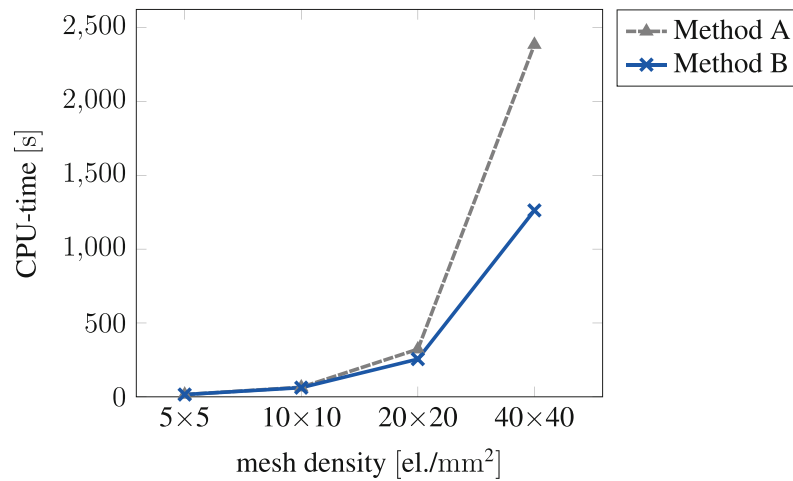


FIGURE 22 Comparison of the runtime of method A and B. Structured meshes are employed in the simulation with $\Delta t = 0.34483$ s.

Furthermore, the runtime of method A and B are compared in this example for different element densities in Figure 22. For coarse meshes, both methods yield similar runtimes (5×5 el./mm², 10×10 el./mm²). But already for the second finest mesh (20×20 el./mm²), method B is with 20.8 % significantly faster than method A. For the finest mesh (40×40 el./mm²), the savings in computation time are 47.1 %.

Moreover, Figure 23 shows the evolution of the dissolution level d , the electric potential v and the electric current density \mathbf{j} of the problem for two intermediate and the final configuration. Inside the cathode, the electric potential is $v = 0$ V and inside the anode $v \approx 10$ V with a transition zone in the electrolyte. The electric current density initially

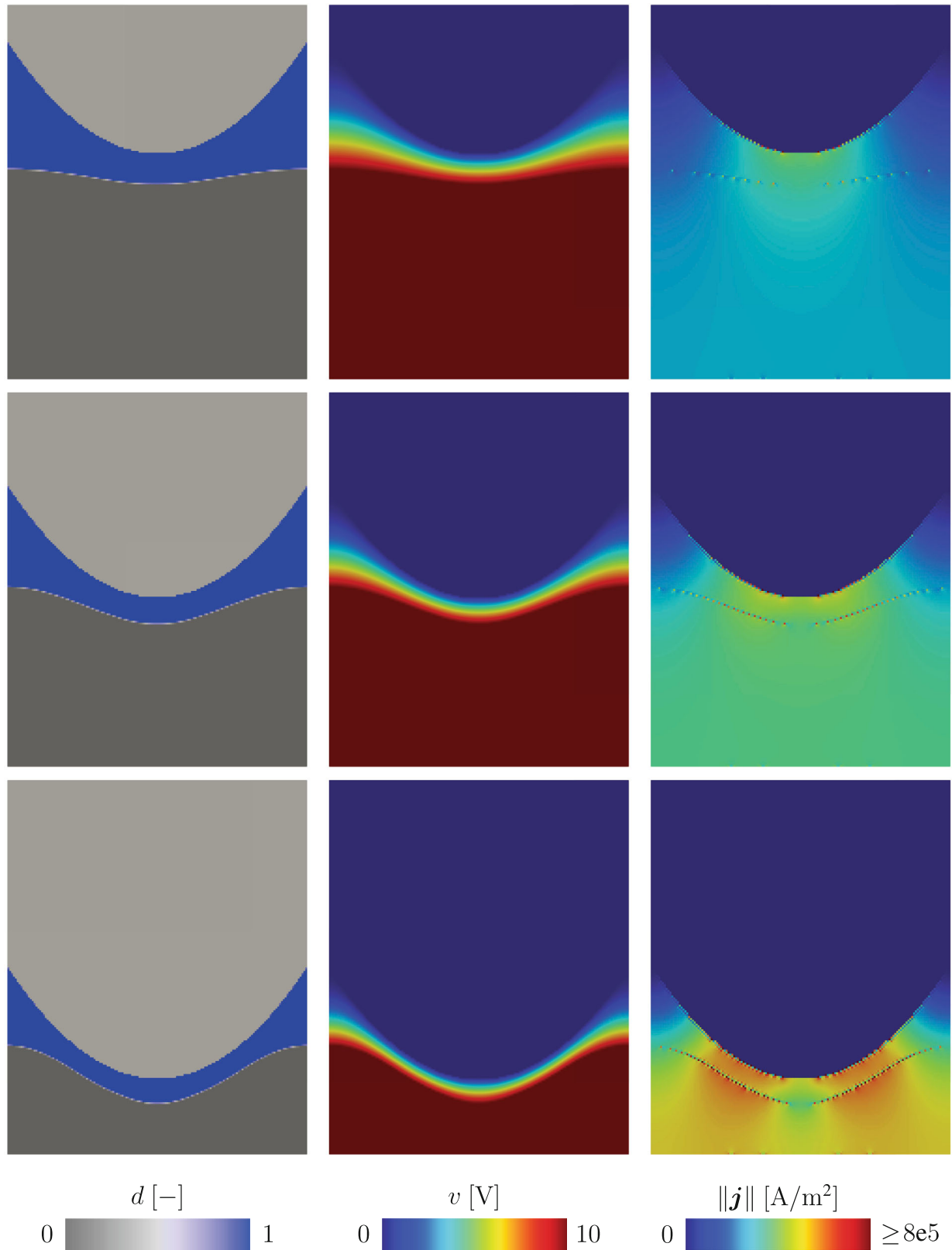


FIGURE 23 Evolution of the dissolution level d , the electric potential v and the norm of the electric current density $\|j\|$ for the parabolic cathode at time steps 100, 250 and 500. Due to varying dissolution levels and cathode ratios in adjacent elements, the visualization of the electric current density may yield minor non-uniformities on the surface of the anode and cathode.

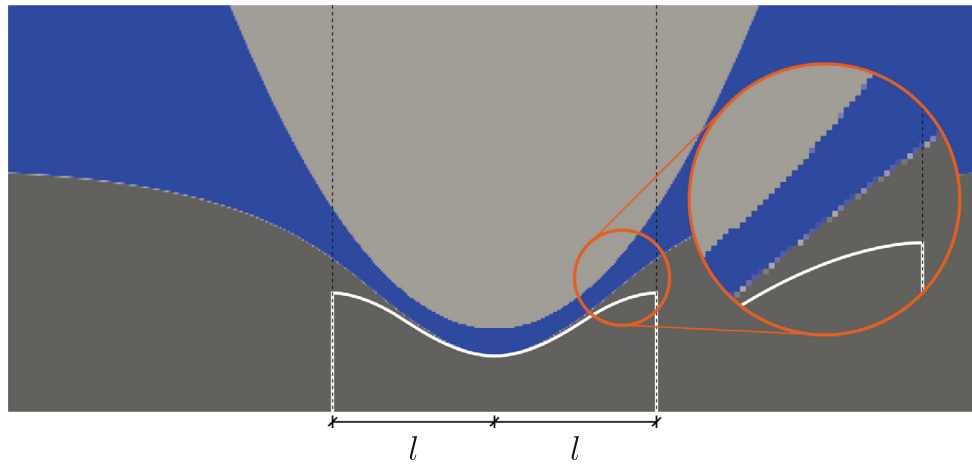


FIGURE 24 Influence of specimen's length in x -direction on final surface shape. The white line shows the final surface of the specimen with a length of $2l$. The contour plot shows the surface of the specimen with a length of $10l$ in the range of $x \approx \pm 3l$.

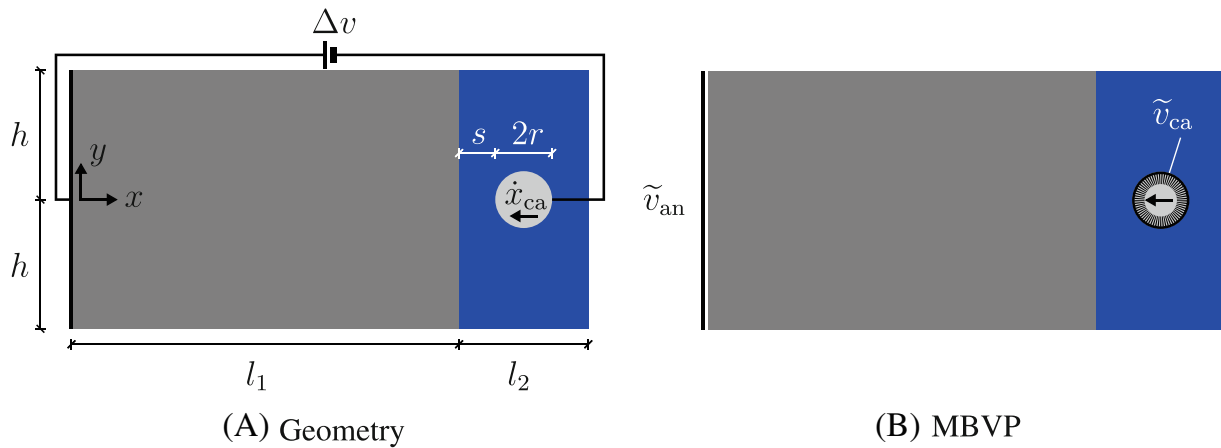


FIGURE 25 Geometry and moving boundary value problem for a wire tool (cf. Reference 36).

concentrates in the middle of the specimen leading to a pronounced material removal in this region. With progressing cathode feed, the electric current density's focus widens mapping a parabolic shape onto the anode.

As discussed in Reference 34 and derived in Reference 35, a parabolic tool yields a parabolic workpiece. In the current example, a flattening of the workpiece's surface at the outer edges is observed. The electric field lines are passing perpendicular to the anode's surface. Here, a zero horizontal flux is prescribed by the Neumann boundary conditions at the outer edge, which, therefore, leads to the flattening of the surface profile in this domain. Figure 24 shows the machined profile of the specimen with a total length of $10l$. The specimen's extension releases the zero flux condition at $x = \pm l$ and avoids the pronounced flattening at this position.

6.3 | Wire cathode - Sharma et al.³⁶

In the third example, a wire electrochemical machining application is investigated (Figure 25) and the results are compared with the experiments and simulations of Reference 36. The geometric dimensions read $l_1 = 700 \mu\text{m}$, $l_2 = 50 \mu\text{m}$, $h = 200 \mu\text{m}$, $s = 10 \mu\text{m}$, $r = 15 \mu\text{m}$ with a thickness of $100 \mu\text{m}$. The feed rate is $\dot{x}_{ca} = 4 \mu\text{m/s}$, the potential difference $\Delta v = 6 \text{ V}$ and the electric conductivity $k_E^{\text{EL}} = 1.71 \text{ A/(V m)}$. We set $v_{\text{dis}} = 1.09 \times 10^{-11} \text{ m}^3/(\text{As})$ and $\Delta t = 0.1 \text{ s}$. This example necessitates the use of method B to apply the cathode condition $\tilde{v}_{ca} = 0 \text{ V}$ only locally within the wire.

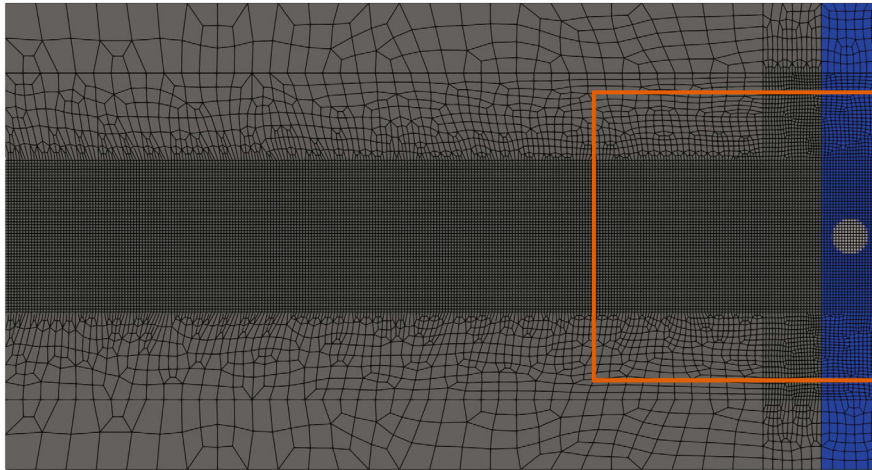


FIGURE 26 Mesh for wire tool example (19995 elements). The orange box indicates the image section investigated in Figure 27.

Figure 26 shows the mesh employed in the simulation which possesses strong refinement in the region of the kerf. Moreover, the orange box in Figure 26 shows the image section of Figure 27 where the initial phase of the dissolution process is studied. Here, the dissolution level d and the norm of the electric current density $\|\mathbf{j}\|$ are given. Initially, the electric current density exhibits its maximum in horizontal direction, thereby, inducing the highest material removal at this position. Afterwards, the electric current density's scope becomes larger which causes a widening of the kerf. After 25 s, the distribution of the electric current density between wire and work piece remains approximately constant and yields a clean cut.

Figure 28 shows the final shape of the specimen after a machining time of 150 s. Measuring the kerf width at $x = 400 \mu\text{m}$ yields a width of $118.73 \mu\text{m}$ which is in the range between $110.08 \mu\text{m}$ (experimental kerf width) and $124.27 \mu\text{m}$ (simulated kerf width) of Reference 36.

The simulation required 10 h 21 min and, thus, was faster than the simulation with the fine discretization of Reference 36 whose code was implemented in MATLAB (R2016a) and required 16 h 03 min. Further speedups are realized by considering an additional moving anode boundary condition. This prescribes $\tilde{v}_{\text{an}} = 6 \text{ V}$ in the region $50 \mu\text{m}$ below the work piece's initial surface and moves horizontally with the cathode's feed rate (Figure 29). The introduction of an additional anode boundary condition to reduce the number of free degrees of freedom was motivated by the assumption that the drop of the electric potential in the workpiece is almost negligible due to the metal's high electric conductivity compared to the electrolyte's relatively low conductivity. Hereby, the computation time is reduced by 59 % to 4 h 28 min and is even faster than the simulation with the coarse discretization of Reference 36 with 6 h 19 min. In this example, prescribing additional anode boundary conditions apparently yields a significant speedup with respect to the computation time without having an influence on the kerf's final shape. This procedure is, however, not applicable to all boundary value problems and should be applied carefully.

6.4 | Complex cathode - blade machining

Inspired by e.g. References 37, 38 or 39, we study in this example a blade machining process with a complex cathode geometry, where two tools move towards an enclosed workpiece.

The material parameters stem from Table 2 and the geometric dimensions (in [mm]) read $l_1 = 4.5$, $s_1 = 1.5$, $l_2 = 10$, $s_2 = 0.35$, $l_3 = 5.65$, $h = 25$ with a thickness of 0.2 (Figure 30). Moreover, the following circles define the cathode's surface with $r_1 = 0.5$ (center: $4 \mid 0.551$), $r_2 = 2$ (center: $4.5 \mid 3$), $r_9 = 0.49$ (center: $16.840 \mid 0.551$). Additionally, the following ellipses complete the surface with $r_3 = 2.8$, $r_4 = 14$ (center: $1.56 \mid 13.9$, rotation: $\alpha_1 = 5.44^\circ$), $r_5 = 11.25$, $r_6 = 4.5$ (center: $16.05 \mid 13.75$, rotation: $\alpha_2 = 11.5^\circ$) and $r_7 = 7.5$, $r_8 = 4.5$ (center: $16.35 \mid 8.5$).

The feed rate is $\dot{x}_{\text{ca}} = 0.01 \text{ mm/s}$ and the potential difference $\Delta v = 20 \text{ V}$ with $\tilde{v}_{\text{an}} = 20 \text{ V}$ which is prescribed in the region $x \in [11.5, 12]$ and $y \in [3, 20]$. The time increment reads $\Delta t = 2 \text{ s}$ and method B is utilized.

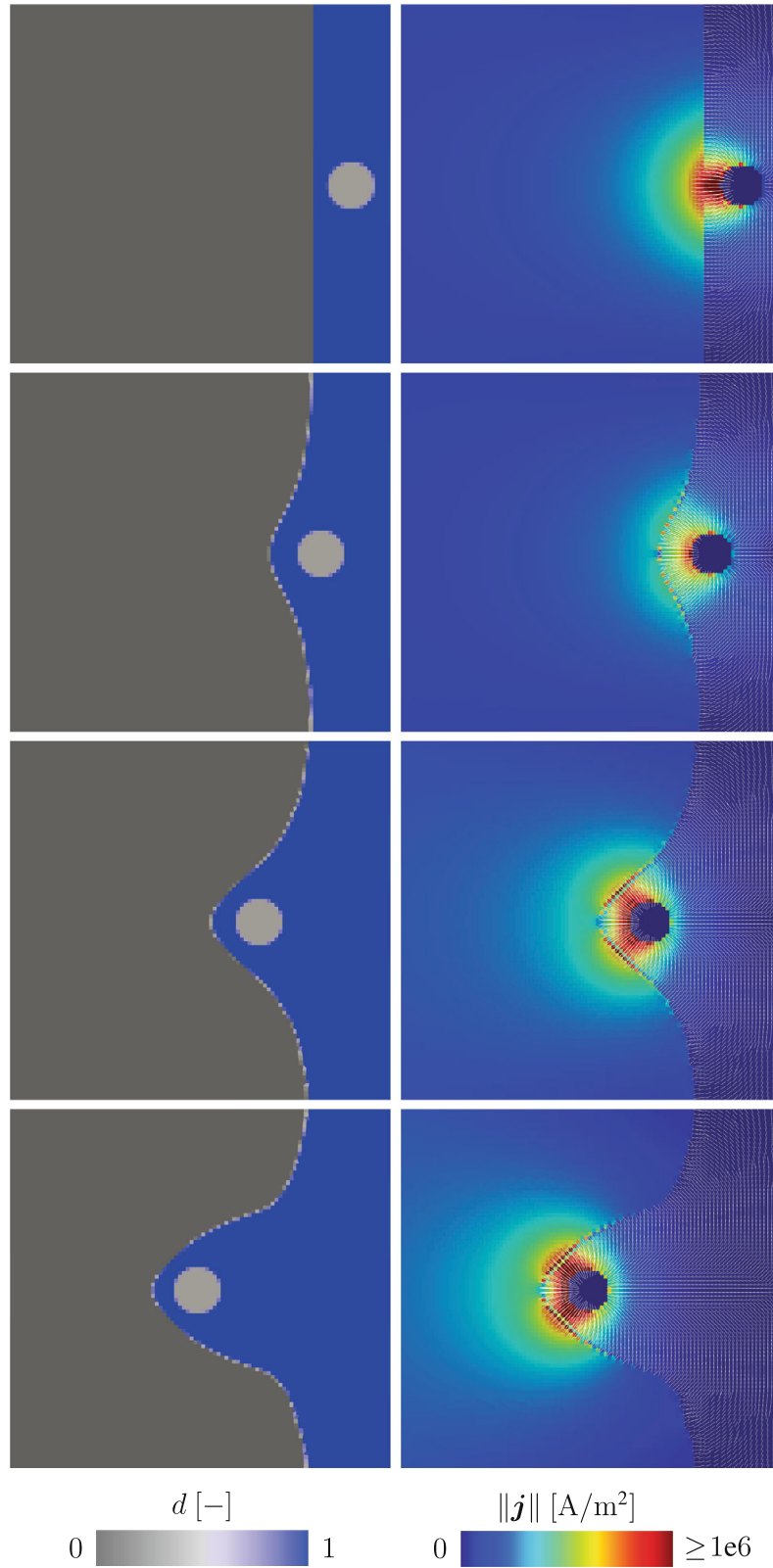


FIGURE 27 Evolution of the dissolution level d and the norm of the electric current density $\|j\|$, where the white lines show the orientation of the electric field, for the wire tool. Zoom to the right edge of the specimen at time 0 s, 5 s, 15 s and 25 s.

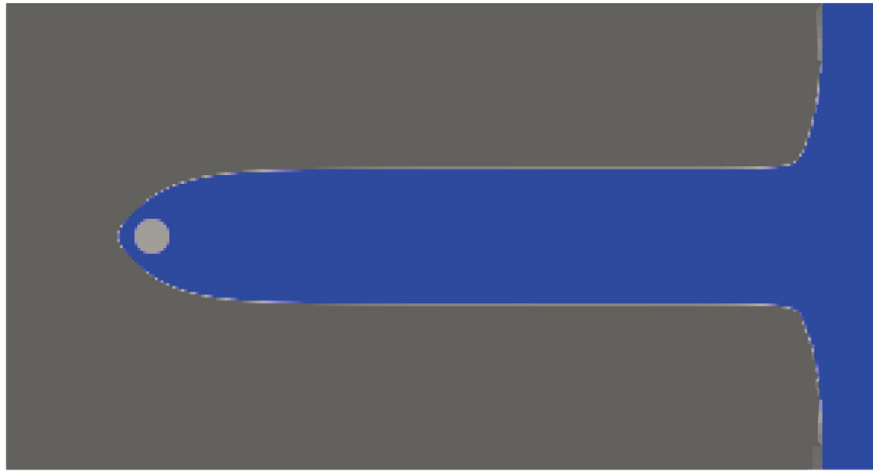


FIGURE 28 Final shape of the specimen after machining with the wire tool after a machining time of 150 s.

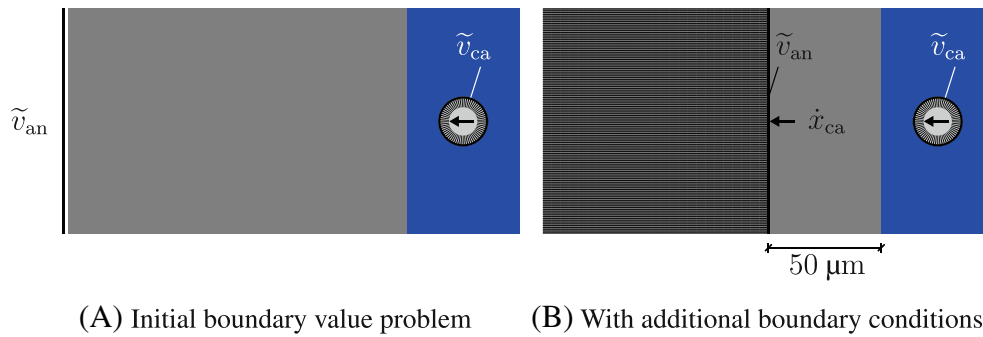


FIGURE 29 Illustration of an additional anode boundary condition 50 μm below the workpiece's surface that moves horizontally with the cathode's feed rate \dot{x}_{ca} . In the shaded area, the electric potential \tilde{v}_{an} is universally applied.

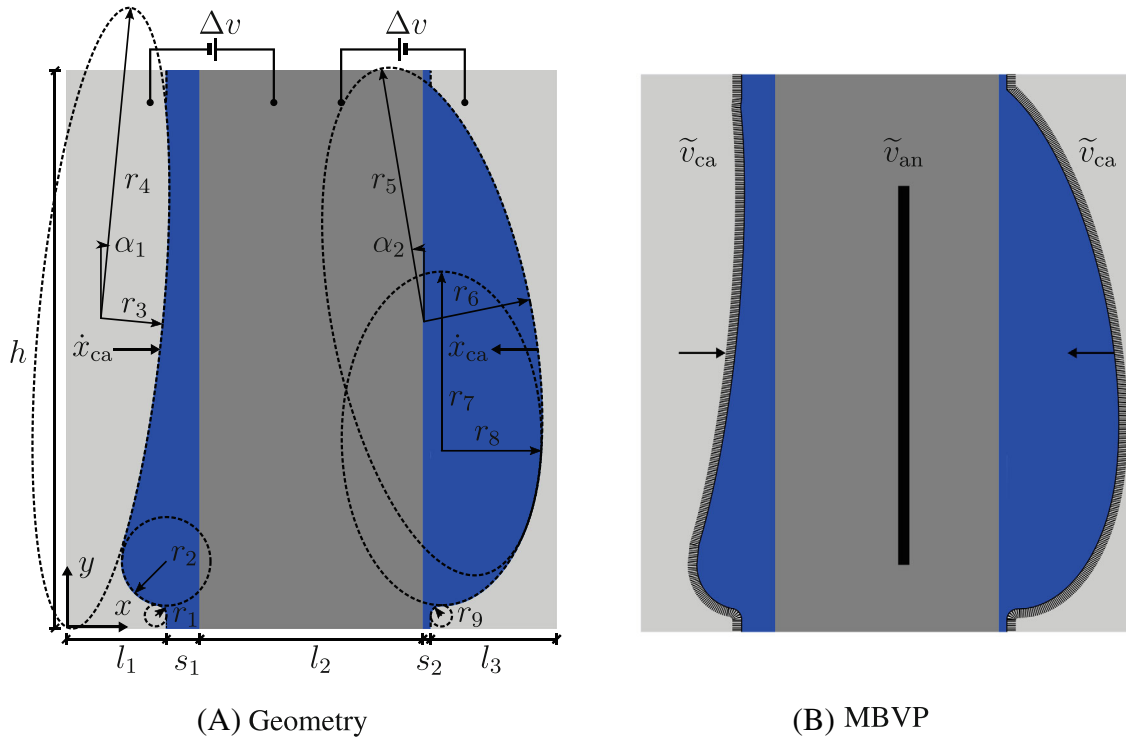


FIGURE 30 Geometry and moving boundary value problem with complex cathode shape.

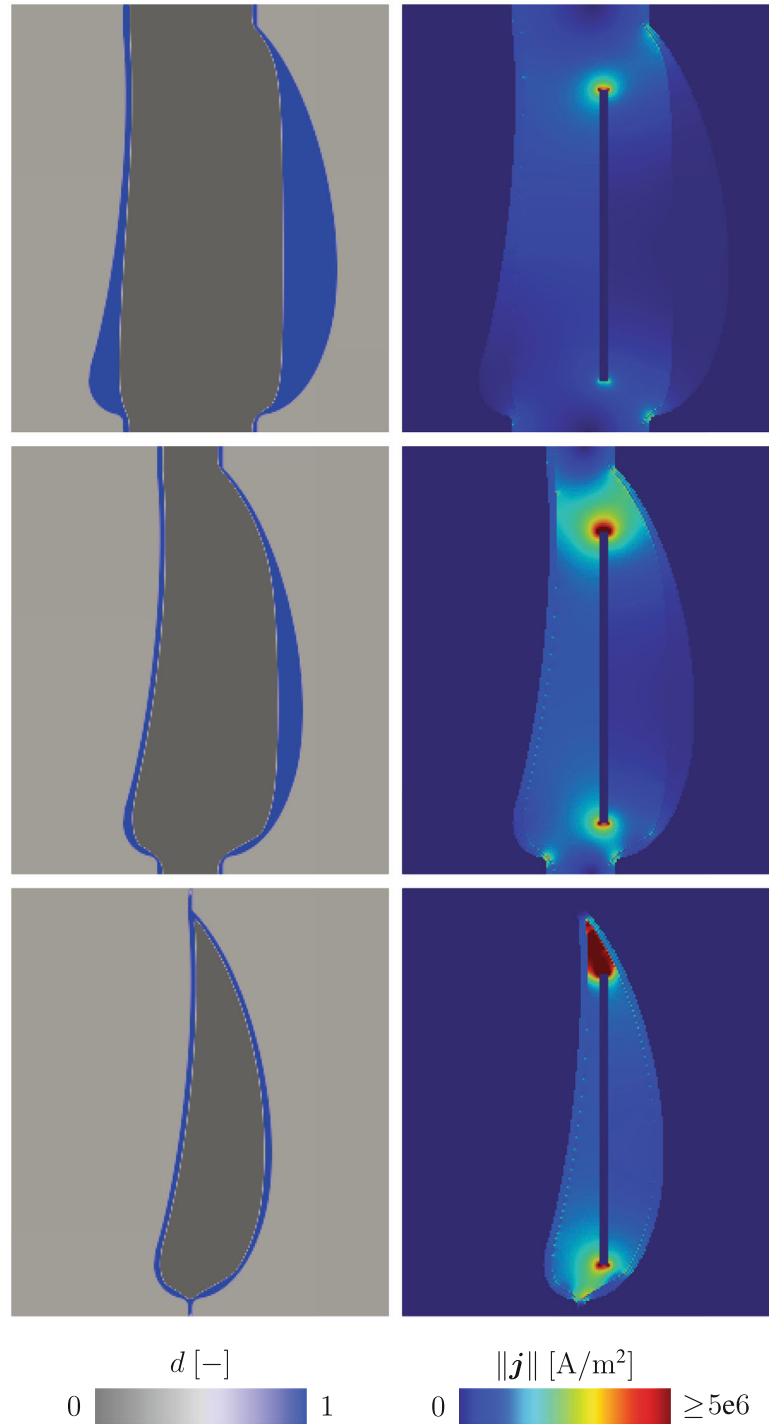


FIGURE 31 Evolution of the dissolution level d and the norm of the electric current density $\|j\|$ for a complex cathode at times 200 s, 400 s and 580 s.

In Figure 31, the evolution of the dissolution level d and the norm of the electric current density $\|j\|$ is presented for two intermediate and the final configuration. Due to the initially small working gap width at the top and bottom region of the specimen, we observe a pronounced material removal in these sections. With increasing machining time, the workpiece continuously dissolves also in the middle of the specimen (time 400 s) until finally the mapping of the cathode's shape onto the workpiece is completed (time 580 s).

The simulation required a computation time of 2 h 6 min and, thus, confirms the method's ability to model complex dissolution processes with good efficiency.

7 | CONCLUSION

In this paper, a novel methodology to model the cathode feed in the moving boundary value problem of electrochemical machining was presented. Two approaches are investigated to describe the cathode. In method A, which is characterized by a simple and robust implementation, the electric conductivities of cathode elements are modified. In method B, Dirichlet boundary conditions are applied on all nodes within the cathode and, hence, facilitate considerable speedups. Elements on the cathode's surface are described by effective material parameters. The model's accuracy is confirmed by analytical as well as experimental and numerical reference solutions from the literature. Moreover, low runtimes allow for the efficient investigation of complex shapes.

The presented model formulation focuses on the efficient description of the cathode feed in ECM simulations. Currently, it considers only certain aspects of the multiphysical process. Thus, further work includes the modeling of multiphase materials (cf. References 40, 41) and the formation of oxide layers (e.g. Reference 42) to incorporate the polarization voltage. Moreover, a formulation of the dissolution model in the gradient enhanced framework, which was introduced by References 43-45 and applied in e.g. References 46,47 can be investigated. Additionally, the numerical efficiency could be further improved by advanced finite element technology using reduced integration methods (cf. References 48,49), where the material law is only evaluated in a single integration point, see e.g. Reference 50 for the treatment of the electric current density with reduced integration. Also the extension to an induced anisotropic electric conductivity formulation due to oxide layers in analogy to anisotropic damage formulations (cf. References 51-53) promises a worthwhile modification. Furthermore, the consideration of mass transfer, hydrogen generation and fluid mechanical effects following References 54-56 would yield a valuable model extension.

Finally, a transfer of the modeling technique to laserchemical machining (LCM, e.g. Reference 57) is aspired, which requires to adapt the evolution equation of the dissolution level from an electrically to a thermally based formulation.⁵⁸

ACKNOWLEDGMENTS

The authors would like to thank the anonymous reviewer for the constructive and helpful feedback. Furthermore, we would like to thank the subproject F03 of the transregional Collaborative Research Center 136 "Process Signatures" for the discussions and for providing material parameter data. Funding granted by the German Research Foundation (DFG) for projects number 453715964, 223500200 (M05) and 417002380 (A01) is gratefully acknowledged. Open Access funding enabled and organized by Projekt DEAL.

DATA AVAILABILITY STATEMENT

The data that support the findings of this study are available from the corresponding author upon reasonable request.

ENDNOTES

*Due to the lack of experimental data, the values of ϵ_r^{CAT} and ϵ_r^{ME} were chosen arbitrarily and have to be determined experimentally in future works.

†Please note that in Reference 21, the values of ϵ_r^{EL} and ϵ_r^{ME} were inadvertently interchanged.

ORCID

Tim van der Velden  <https://orcid.org/0000-0001-8054-5091>

REFERENCES

1. Klocke F, Klink A, Veselovac D, et al. Turbomachinery component manufacture by application of electrochemical, electro-physical and photonic processes. *CIRP Ann.* 2014;63(2):703-726.
2. DeBarr AE, Oliver DA. *Electrochemical Machining*. Macdonald & Co. Ltd; 1968.
3. McGeough JA. *Principles of Electrochemical Machining*. Chapman & Hall; 1974.
4. Klocke F, König W. *Fertigungsverfahren 3 Abtragen, Generieren und Lasermaterialbearbeitung*. Springer; 2007.
5. Rajurkar KP, Sundaram MM, Malshe AP. Review of electrochemical and electrodischarge machining. *Procedia CIRP*. 2013;6:13-26.
6. Hinduja S, Kunieda M. Modelling of ecm and edm processes. *CIRP Ann.* 2013;62(2):775-797.
7. Tipton H. The dynamics of electrochemical machining. Paper presented at: Proc. 5th Int. MTDR Conf; University of Birmingham, Birmingham; 1964:509-522.
8. Koenig W, Huembs HJ. Mathematical model for the calculation of the contour of the anode in electrochemical machining. *Ann CIRP*. 1977;25:83-87.
9. Kozak J. Mathematical models for computer simulation of electrochemical machining processes. *J Mater Process Technol*. 1998;76:170-175.

10. Christiansen S, Rasmussen H. Numerical solutions for two-dimensional annular electrochemical machining problems. *J Inst Math Appl*. 1976;18:295-307.
11. Fasano A, Primicerio M. *Free Boundary Problems: Theory and Applications*. Vol 2. Pitman Advanced Publishing Program; 1983.
12. Deconinck J, Maggetto G, Vereecken J. Calculation of current distribution and electrode shape change by the boundary element method. *J Electrochem Soc*. 1985;132(12):2960-2965.
13. Narayanan OH, Hinduja S, Noble CF. The prediction of workpiece shape during electrochemical machining by the boundary element method. *Int J Mach Tool Des Res*. 1986;26(3):323-338.
14. Alkire R, Bergh T, Sani RL. Predicting electrode shape change with use of finite element methods. *J Electrochem Soc*. 1978;125(12):1981-1988.
15. Jain VK, Pandey PC. Finite element approach to the two dimensional analysis of electrochemical machining. *Precis Eng*. 1980;2(1):23-28.
16. Hardisty H, Mileham AR, Shirvarni H, Bramley AN. A finite element simulation of the electrochemical machining process. *CIRP Ann*. 1993;42(1):201-204.
17. Brookes D. *Computer-Aided Shape Prediction of Electro-chemically Machined Work Using the Method of Finite Elements*. The University of Manchester (PhD Thesis); 1984.
18. Deconinck D, Van Damme S, Albu C, Hotoiu L, Deconinck J. Study of the effects of heat removal on the copying accuracy of the electrochemical machining process. *Electrochim Acta*. 2011;56(16):5642-5649.
19. Wuilbaut TA. *Algorithmic Developments for a Multiphysics Framework*. (Unpublished doctoral dissertation). Université libre de Bruxelles, Faculté des sciences appliquées – Mécanique, Bruxelles; 2008.
20. Klocke F, Heidemanns L, Zeis M, Klink A. A novel modeling approach for the simulation of precise electrochemical machining (pecm) with pulsed current and oscillating cathode. *Procedia CIRP*. 2018;68:499-504.
21. van der Velden T, Rommes B, Klink A, Reese S, Waimann J. A novel approach for the efficient modeling of material dissolution in electrochemical machining. *Int J Solids Struct*. 2021;229:111106 ISSN 0020-7683.
22. Antonova EE, Looman DC. Finite elements for thermoelectric device analysis in ansys. Paper presented at: IEEE. ICT 2005. 24th International Conference on Thermoelectrics; 2005:215-218.
23. Pérez-Aparicio JL, Taylor RL, Gavela D. Finite element analysis of nonlinear fully coupled thermoelectric materials. *Comput Mech*. 2007;40(1):35-45.
24. Hofmann T, Westhoff D, Feinauer J, et al. Electro-chemo-mechanical simulation for lithium ion batteries across the scales. *Int J Solids Struct*. 2020;184:24-39.
25. Wu T, Li H. Phase-field model for liquid-solid phase transition of physical hydrogel in an ionized environment subject to electro-chemo-thermo-mechanical coupled field. *Int J Solids Struct*. 2018;138:134-143.
26. Liu Q, Liu M, Li H, Lam KY. Multiphysics modeling of responsive deformation of dual magnetic-ph-sensitive hydrogel. *Int J Solids Struct*. 2020;190:76-92.
27. Jackson JD. *Classical Electrodynamics*. John Wiley & Sons Ltd; 1962.
28. Kachanov LM. Time of the rupture process under creep conditions. *TVZ Akad Nauk S.S.R Otd Tech. Nauk*. 1958;8:26-31.
29. Schwab AJ. *Begriffswelt der Feldtheorie*. 8th ed. Springer Vieweg Berlin; 2019.
30. Hughes TJR. *The Finite Element Method: Linear Static and Dynamic Finite Element Analysis*. Prentice Hall; 1987.
31. Zienkiewicz OC, Taylor RL, Zhu JZ. *The Finite Element Method: Its Basis and Fundamentals*. Elsevier; 2005.
32. Taylor RL, Govindjee S. *FEAP - A Finite Element Analysis Program*. University of California; 2020 http://projects.ce.berkeley.edu/feap/manual_86.pdf
33. Joe B. Geompack—a software package for the generation of meshes using geometric algorithms. *Adv Eng Softw Workstations*. 1991;13(5-6):325-331.
34. Hardisty H, Mileham AR. Finite element computer investigation of the electrochemical machining process for a parabolically shaped moving tool eroding an arbitrarily shaped workpiece. *Proc Inst Mech Eng B: J Eng Manuf*. 1999;213(8):787-798.
35. Nilson RH, Tsuei YG. Free boundary problem for the laplace equation with application to ECM tool design. *J Appl Mech*. 1976;43(1):54-58.
36. Sharma V, Srivastava I, Jain VK, Ramkumar J. Modelling of wire electrochemical micromachining (wire-ecmm) process for anode shape prediction using finite element method. *Electrochim Acta*. 2019;312:329-341.
37. Tsuboi R, Yamamoto M. Modeling and applications of electrochemical machining process. *ASME Int Mech Eng Congress Expo*. 2009;4:377-384.
38. Klocke F, Zeis M, Harst S, Klink A, Veselovac D, Baumgärtner M. Modeling and simulation of the electrochemical machining (ecm) material removal process for the manufacture of aero engine components. *Procedia CIRP*. 2013;8:265-270.
39. Zhu D, Zhao J, Zhang R, Yu L. Electrochemical machining of blades with cross-structural cathodes at leading/trailing edges. *Int J Adv Manuf Technol*. 2017;93(9):3221-3228.
40. Kozak J, Zybura-Skrabalak M. Some problems of surface roughness in electrochemical machining (ecm). *Procedia CIRP*. 2016;42:101-106.
41. Harst S. *Entwicklung Einer Prozesssignatur für die Elektrochemische Metallbearbeitung*. Apprimus Wissenschaftsverlag; 2019.
42. Zander D, Schupp A, Beyss O, Rommes B, Klink A. Oxide formation during transpassive material removal of martensitic 42CrMo4 steel by electrochemical machining. *Mater*. 2021;14(2):402.
43. Dimitrijevic BJ, Hackl K. A method for gradient enhancement of continuum damage models. *Tech Mech-Eur J Eng Mech*. 2008;28(1):43-52.

44. Forest S. Micromorphic approach for gradient elasticity, viscoplasticity, and damage. *J Eng Mech.* 2009;135(3):117-131.
45. Forest S. Nonlinear regularization operators as derived from the micromorphic approach to gradient elasticity, viscoplasticity and damage. *Proc R Soc A: Math Phys Eng Sci.* 2016;472(2188):20150755.
46. Kiefer B, Waffenschmidt T, Sprave L, Menzel A. A gradient-enhanced damage model coupled to plasticity—multi-surface formulation and algorithmic concepts. *Int J Damage Mech.* 2018;27(2):253-295.
47. Junker P, Schwarz S, Jantos DR, Hackl K. A fast and robust numerical treatment of a gradient-enhanced model for brittle damage. *Int J Multiscale Comput Eng.* 2019;17(2):151-180.
48. Zienkiewicz OC, Taylor RL, Too JM. Reduced integration technique in general analysis of plates and shells. *Int J Numer Methods Eng.* 1971;3(2):275-290.
49. Hughes TJR, Cohen M, Haroun M. Reduced and selective integration techniques in the finite element analysis of plates. *Nuclear Eng Des.* 1978;46(1):203-222.
50. Reese S, Svendsen B, Stiemer M, Unger J, Schwarze M, Blum H. On a new finite element technology for electromagnetic metal forming processes. *Arch Appl Mech.* 2005;74(11):834-845.
51. Langenfeld K, Mosler J. A micromorphic approach for gradient-enhanced anisotropic ductile damage. *Comput Methods Appl Mech Eng.* 2020;360:112717.
52. Dorn C, Wulfinghoff S. A gradient-extended large-strain anisotropic damage model with crack orientation director. *Comput Methods Appl Mech Eng.* 2021;387:114123.
53. Holthusen H, Brepols T, Reese S, Simon J-W. A two-surface gradient-extended anisotropic damage model using a second order damage tensor coupled to additive plasticity in the logarithmic strain space. *J Mech Phys Solids.* 2022;163:104833.
54. Deconinck D, Van Damme S, Deconinck J. A temperature dependent multi-ion model for time accurate numerical simulation of the electrochemical machining process. Part i: theoretical basis. *Electrochim Acta.* 2012a;60:321-328. ISSN 0013-4686.
55. Deconinck D, Van Damme S, Deconinck J. A temperature dependent multi-ion model for time accurate numerical simulation of the electrochemical machining process. Part ii: numerical simulation. *Electrochim Acta.* 2012b;69:120-127. ISSN 0013-4686.
56. Deconinck D, Hoogsteen W, Deconinck J. A temperature dependent multi-ion model for time accurate numerical simulation of the electrochemical machining process. Part iii: experimental validation. *Electrochim Acta.* 2013;103:161-173. ISSN 0013-4686.
57. Schupp A, Pütz RD, Beyss O, Beste L-H, Radcl T, Zander D. Change of oxidation mechanisms by laser chemical machined rim zone modifications of 42crmo4 steel. *Mater.* 2021;14(14):3910.
58. Klocke F, Vollertsen F, Harst S, et al. Comparison of material modifications occurring in laserchemical and electrochemical machining. *Proc INSECT.* 2016;12:57-63.

How to cite this article: van der Velden T, Ritzert S, Reese S, Waimann J. A novel numerical strategy for modeling the moving boundary value problem of electrochemical machining. *Int J Numer Methods Eng.* 2023;1-27. doi: 10.1002/nme.7190

APPENDIX A

A.1 Derivation of the weak form

We start from the local form of the balance equation, Equation (1-1),

$$\dot{\rho}_E + \text{div}(\mathbf{j}) = 0$$

where we insert Gauss' law of electrostatics with $\rho_E = \text{div}(\mathbf{D}) = \text{div}(\epsilon_0 \epsilon_r \mathbf{E})$ into $\dot{\rho}_E$ leading to

$$\text{div}(\epsilon_0 \epsilon_r \dot{\mathbf{E}} + \mathbf{k}_E \mathbf{E}) = 0. \quad (\text{A1})$$

This equation is multiplied by the test function δv , which is 0 on Γ_v and otherwise arbitrary and which can also be interpreted as variation of v , and is then integrated over the domain Ω

$$\int_{\Omega} \text{div}(\epsilon_0 \epsilon_r \dot{\mathbf{E}} + \mathbf{k}_E \mathbf{E}) \delta v \, dV = 0. \quad (\text{A2})$$

Next, the integration by parts is considered with $\text{div}(\mathbf{b}) \, a = -\mathbf{b} \cdot \text{grad}(a) + \text{div}(\mathbf{b} \, a)$ leading to

$$-\int_{\Omega} (\epsilon_0 \epsilon_r \dot{\mathbf{E}} + \mathbf{k}_E \mathbf{E}) \cdot \text{grad}(\delta v) \, dV + \int_{\Omega} \text{div}((\epsilon_0 \epsilon_r \dot{\mathbf{E}} + \mathbf{k}_E \mathbf{E}) \delta v) \, dV = 0. \quad (\text{A3})$$

Then, we apply the divergence theorem and obtain

$$-\int_{\Omega} (\epsilon_0 \epsilon_r \dot{\mathbf{E}} + \mathbf{k}_E \mathbf{E}) \cdot \text{grad}(\delta v) \, dV + \underbrace{\int_{\Gamma_j} (\epsilon_0 \epsilon_r \dot{\mathbf{E}} + \mathbf{k}_E \mathbf{E}) \cdot \mathbf{n} \, \delta v \, dA}_{=: g_j} = 0, \quad (\text{A4})$$

where the surface integral is abbreviated by g_j , thus, leading to the weak form of Equation (4)

$$g_v := -\int_{\Omega} (\epsilon_0 \epsilon_r \dot{\mathbf{E}} + \mathbf{k}_E \mathbf{E}) \cdot \text{grad}(\delta v) \, dV + g_j.$$